A phenotype-structured model to reproduce the avascular growth of a tumor and its interaction with the surrounding environment

A phenotype-structured model to reproduce the avascular growth of a tumor and its interaction with the surrounding environment

Giada Fiandaca[a,*,1], Sara Bernardi[a,2], Marco Scianna[a,3] and Marcello Edoardo Delitala[a,4]

[a]*Department of Mathematical Sciences "G. L. Lagrange", Politecnico di Torino, Corso Duca degli Abruzzi 24, 10129 Torino, Italy*

ARTICLE INFO

Keywords:
tumor growth
phenotype-structured model
tumor phenotypic heterogeneity
necrosis
parabolic partial differential equations

ABSTRACT

We here propose a one-dimensional spatially explicit phenotype-structured model to analyze selected aspects of avascular tumor progression. In particular, our approach distinguishes viable and necrotic cell fractions. The metabolically active part of the disease is, in turn, differentiated according to a continuous trait, that identifies cell variants with different degrees of motility and proliferation potential. A parabolic partial differential equation (PDE) then governs the spatio-temporal evolution of the phenotypic distribution of active cells within the host tissue. In this respect, active tumor agents are allowed to duplicate, move upon haptotactic and pressure stimuli, and eventually undergo necrosis. The mutual influence between the emerging malignancy and its environment (in terms of molecular landscape) is implemented by coupling the evolution law of the viable tumor mass with a parabolic PDE for oxygen kinetics and a differential equation that accounts for local consumption of extracellular matrix (ECM) elements. The resulting numerical realizations reproduce tumor growth and invasion in a number scenarios that differ for cell properties (i.e., individual migratory behavior, duplication and mutation potential) and environmental conditions (i.e., level of tissue oxygenation and homogeneity in the initial matrix profile). In particular, our simulations show that, in all cases, more mobile cell variants occupy the front edge of the tumor, whereas more proliferative clones are selected at the more internal regions. A necrotic core constantly occupies the bulk of the mass due to nutrient deprivation. This work may eventually suggest some biomedical strategies to partially reduce tumor aggressiveness, i.e., to enhance necrosis of malignant tissue and to promote the presence of more proliferative cell phenotypes over more invasive ones.

Carcinogenesis is a multistage process that arises from a genetic mutation or a epigenetic alteration that occurs in a small node of cells (typically somatic stem individuals (Cristini and Lowengrub (2010)) and is able to escape from DNA repair mechanisms (Osada and Takahashi (2002)). The damaged cells undergo uncontrolled proliferation and acquire over time further malfunctions, that allow them also to ignore growth-inhibiting signals from the neighbors or from the environment (Hanahan and Weinberg (2011)). A sphere-like hyper-proliferative colony then forms and establishes a foothold in the host normal tissue (Alberts et al. (2002)). Such primary tumor continues to grow *in situ*: however, the increment in cell mass due to aberrant mitosis causes acute and chronic lack of oxygen and nutrients as well as increase of metabolites, see the reviews Harris (2002); Lowengrub et al. (2009) and references therein. The existing vasculature is often inadequate to deliver the needed substrates: such harsh conditions indeed induce malignant cells to release selected growth factors that drive *angiogenesis*, i.e., formation of new vessels by extension from the main circulatory system. Once the malignancy is vascularized, it can further progress and even shed cells into the vasculature, or in the lymphatic system (intravasation): such individuals may survive, escape from the circulation (extravasation) and then establish satellite clusters in distant parts of the host body (Abramovitch et al. (1995)). The new colonies may finally begin to grow to form secondary lesions. Such a phenomenon, called *metastatization*, is the predominant cause of mortality due to cancer (Mehlen and Puisieux (2006); Lowengrub et al. (2009)).

Malignant angiogenesis is not the only mechanism that promotes metastatic phenomena. In fact, small clusters of tumor cells may scatter from the original mass, invade the surrounding tissue, and continue their migration into the preexisting circulation (Hanahan and Weinberg (2011)). In these early stages of progression, i.e., before vascular transition, tumor growth and expansion within the host rely on collective cell dynamics. As commented in the review by Lowengrub and coworkers, motion of more or less dense cell aggregates in fact dominates in a wide range of

*Corresponding author
ORCID(s): 0000-0002-7923-5878 (G. Fiandaca)
[1]giada.fiandaca@polito.it
[2]sara.bernardi@polito.it
[3]marco.scianna@polito.it
[4]marcello.delitala@polito.it

tumors whereas invasion by individual cancer agents is more rarely observed. Such a collective migration is facilitated by the emergence of an intratumoral phenotypic heterogeneity. Cells forming a neoplastic tissue have in fact different characteristics and functions and can cooperate to survive and efficiently invade the host. In this respect, several cancer cell phenotypes have been identified: in particular, in Hanahan and Weinberg (2011), the authors distinguish cells characterized by high motility rates from those identified by unlimited proliferative potential. The former variant has been shown to undergo poor mitotic events, to lose epithelial characteristics, such as stable cell-cell adhesion and apico-basal polarity, and to acquire mesenchymal features which allow aggressive migration. The latter subpopulation undergoes dramatically high duplication events, lose migratory freedom and re-acquire epithelial hallmarks, including expression of junctional proteins. Highly mitotic agents further fuel invasion of more motile individuals by exerting oncotic pressure and consuming critical substrate. On the opposite, more invasive cells can open migratory paths for less motile but more death-resistant clones. Such an inverse correlation between cell migratory and mitotic potential, a concept also referred to as the "Go-or-Grow" (GoG) hypothesis, characterizes several types of malignancies, see Giese et al. (1996a,b) and references therein, and has been also successfully employed in the theoretical literature (Hatzikirou et al. (2012); Gallaher et al. (2019); Swanson et al. (2011); Martínez-González et al. (2012); Zhigun et al. (2018)). As demonstrated in Gao et al. (2005), cells may also experience a hybrid status, with intermediate levels of mobility and proliferation ability: this type of individuals is often classified as *generalist* cells (Hausser and Alon (2020)). However, a simultaneous maximization of both characteristics, that would give rise to a *super phenotype*, has not been yet observed (Stearns (1989)).

The internal composition of a tumor relates to its malignancy: for instance, in Giese et al. (1996b,a, 2003), it is reported that most aggressive[5] cancers are characterized by the relevant presence of cells with enhanced motility. More motile cell variants have been also shown to have reduced sensitivity to treatments such as radio- and chemotherapy w.r.t. the highly proliferating ones (Risom et al. (2018); Lefranc et al. (2005); Moore et al. (2012)). Intratumoral heterogeneity can vary either spontaneously or in response to specific cues, in particular, in response to environmental conditions. Tumors can be in fact considered as evolving ecosystems whose component cells can be seen as individuals that proliferate, die, undergo phenotypic variations and compete for space and resources under the selective pressure of the surrounding tissue, see Maley et al. (2017) and references therein. In this respect, at each stage of progression, a malignancy is locally and globally composed of the most adapt cell variants.

A deep understanding of the regulatory dynamics of each phase of tumor development indeed represents a fundamental issue in cancer research. However, the relative importance of the cellular and the molecular processes involved, in particular of the impact of the surrounding environment on the evolution and the heterogeneity of the malignant mass, has not been completely revealed so far. In the last decades a fundamental help has been provided by a wide range of computational approaches, able to realistically reproduce selected features of the biological system and to test potential therapeutic strategies, as pointed out by the excellent reviews Adam (1997); Anderson and Chaplain (1998); Anderson et al. (2000); Anderson and Quaranta (2008); Trucu et al. (2016); Araujo and McElwain (2004); Bellomo et al. (2008); Bellomo and Preziosi (2000); Cristini and Lowengrub (2010); Moreira and Deutsch (2002); Friedman (2004, 2007); Eftimie et al. (2011). Following this line of research, we here propose a one-dimensional spatially explicit phenotype-structured model to investigate the avascular evolution of a tumor, in terms of both overall growth and internal heterogeneity. Our approach allows to distinguish in the malignant mass the viable cell fraction and, eventually, a necrotic region. The metabolically active part of the disease is in turn differentiated according to a trait that identifies cell variants with a distinct degree of motility and proliferation potential, according to the above-introduced "Go-or-Grow" hypothesis. A parabolic partial differential equation (PDE) is then set to describe the spatio-temporal evolution of the phenotypic distribution of viable cells within the host tissue. In particular, we take into account the possibility of cell movement due to pressure effects and to the presence of extracellular matrix gradients, that are known to represent significant guidance cues for invasive cancer (and non cancer) cells. Local variations in the amount and the type of malignant cells are set to depend on the local availability of oxygen and free space. The mutual influence between the emerging tumor and its environment is implemented by coupling the evolution law of the viable tumor mass with (i) a parabolic PDE that governs the local concentration of oxygen including (or not) chemical sources at the edges of the considered tissue and (ii) a differential equation that reproduces consumption of extracellular matrix (ECM) elements from malignant individuals. In this respect, for the sake of simplicity, we here account only for fixed and soluble matrix

[5] *Terminological remark*: throughout this work, we will use the adjective *aggressive* to define the clones of malignant cells that are characterized by high migratory ability and low proliferation rate, i.e., those that in principle have the highest metastatic potential. Coherently, we will classify as *aggressive* the tumors characterized by the predominant presence of such cell phenotypes, even if the malignant mass is formed by a low number of component individuals.

components, despite ECMs forming connective tissues are also composed of insoluble collagenous fibers, that however play a key role in cell migration, specially in three-dimensional settings. As modeling results, we first show the ability of our approach to recapitulate some of the main aspects of avascular tumor growth, which are mathematically quantified through suitable observables. We then turn to systematically assess the effect on tumor evolution and on its internal heterogeneity of variations both in cell biophysical/biochemical characteristics and in environmental conditions. The aim is to point out computational settings that result in a malignant mass with a predominant proliferative composition and a poor invasive behavior. Such theoretical outcomes may in fact help in foreseeing the design of efficient treatment strategies. Along the text, we discuss our simulation results in contrast to proper experimental evidence mainly from a qualitative perspective. When possible, quantitative comparisons are proposed as well (for instance, we make sure that the growth rate of our malignant mass falls in a realistic range).

Our approach belongs to the family of models based on the so-called *adaptive dynamics*. As reviewed in Perthame (2006), they are built on the idea that the evolution of an heterogeneous cell population, i.e., structured w.r.t. one or more traits, is mainly driven by selection and mutation. The former favors the diffusion of cell variants with the most adapt phenotype, whereas the latter allows the emergence of offsprings with slightly different determinants with respect to their progenitors. Such a mathematical framework has been recently developed by including the role of abiotic factors in the evolution of a solid tumor (see Lorenzi et al. (2018)) and the possibility of individual movement. In this respect, in Villa et al. (2021); Fiandaca et al. (2021), malignant cells have been assumed to randomly migrate within the host via the introduction of a diffusion term. A more accurate description of individual movement has been introduced in Lorenzi et al. (2020), where the velocity of a given cell fraction has been set to depend on its trait (assuming the already-cited "Go-or-Grow" dichotomy) and on the local pressure.

We here enrich these approaches by introducing some novel aspects:

- the differentiation between viable and necrotic tumor cells, with the possibility of irreversible transitions;
- the dependence of cell movement not only on pressure effects but also on the amount and the distribution of matrix elements;
- the dependence of cell proliferation events on the presence of nutrients and available space, with phenotype-specific rates.

Such modeling developments, according to us, allow a more realistic description of the early evolution of a solid tumor: in particular, the phenotypic composition of the mass is no longer established by an *a priori* fittest trait but emerges as a natural consequence of its interaction with the surrounding environment.

The rest of the paper is organized at it follows: in Section 1, we will present the proposed model with the underlying assumptions. Section 2 will then deal with its numerical implementation. In particular, we will first give details on the parameters estimate and on the indices that will quantity tumor progression. We will then turn to describe the growth of the malignancy in a number of selected settings. The article will end in Section 3 with a summary of the main results, which will be reviewed from a therapeutic perspective. We will finally discuss significant limitations of our approach, with hints for possible developments.

1. Mathematical Model

As sketched in the Introduction, we study avascular growth and evolutionary dynamics of a generic solid tumor with a heterogeneous nature, i.e., formed by cells characterized by different phenotypes. In particular, we focus on the interactions between the nascent malignant mass and selected microenvironmental components, e.g., the oxygen supplied by the pre-existing vasculature and the structural extracellular matrix (ECM). Tumor cells are here allowed to proliferate, compete for limited resources, and infiltrate the tissue. They can also vary their biochemical and biophysical determinants and fall in a necrotic state. Cell behavior and phenotypic characteristics are assumed to be affected by the surrounding molecular landscape, which is in turn influenced by the presence of the disease in a *feedback/feedforward* fashion. The proposed approach is genuinely multiscale: it in fact includes elements evolving at different spatio-temporal levels that directly impact one on each other.

In more details, the above-described pathological system is modeled on a mono-dimensional domain $X = [x_1, x_2] \subset \mathbb{R}$ (x being the space variable), which reproduces a linear cross-section of a tissue with the nascent lesion (left panel in Fig. 1). Tumor growth is then studied for the period $T = [0, t_F] \subset \mathbb{R}_0^+$, t being the time variable.

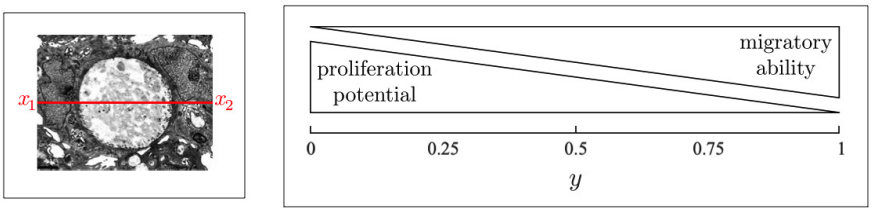

Figure 1: Left panel: the spatial domain X is set to represent a linear section of a tissue with the nascent malignant mass. The experimental image, showing an *in vivo* glioblastoma spheroid, is a courtesy of the Candiolo Cancer Institute (Torino, Italy). Right panel: the active malignant cells are differentiated according to the trait $y \in [0, 1]$, that describes their proliferation and migratory ability. In particular, individuals characterized by $y = 0$ display high duplication potential and poor mobility. On the opposite, a phenotype $y = 1$ identifies cells with substantial migration capacity but negligible proliferation rate.

The population of malignant cells is differentiated in *metabolically active* (i.e., viable) and *necrotic* individuals. The former group is in turn structured with respect to the trait $y \in Y = [0, 1]$, that describes cell migratory and proliferative characteristics in accordance with the "Go-or-Grow" assumption specified in the introductive section. In this respect, as shown in the right panel of Fig. 1, the phenotypic state $y = 0$ defines the cell clone with the highest mitotic potential and the lowest level of mobility, whereas $y = 1$ confers the highest migratory ability but the lowest duplication capacity. Between such extreme values, there is a continuum spectrum of possible states, that implicate the presence of cell variants with intermediate levels of both mobility and proliferation.

According to these hypotheses, the function $a(t, x, y) : T \times X \times Y \mapsto \mathbb{R}_0^+$ hereafter defines the local distribution of active tumor cells on the trait space. In other words, $a(t, x, y)$ reflects the phenotypic composition of the tumor mass located at time t in the domain point x. The number density of viable individuals can be therefore computed as:

$$\rho(t, x) = \int_Y a(t, x, y)\, dy. \tag{1}$$

The overall amount of active cells actually present within the entire domain X can be naturally obtained by integrating the number density $\rho(t, x)$ along the space variable x, i.e., $N_a(t) = \int_X \rho(t, x)\, dx$.

The necrotic subpopulation is instead assumed to be undifferentiated, with number density given by the function $n(t, x) : T \times X \mapsto \mathbb{R}_0^+$. Coherently, $N_n(t) = \int_X n(t, x)\, dx$ gives the total number of necrotic cells present in the tissue. From a biomedical perspective, magnetic resonance imaging (MRI) sequences would locally visualize the overall cell density $\rho + n$.

We finally introduce the field variables $O(t, x), M(t, x) : T \times X \mapsto \mathbb{R}_0^+$ to model oxygen concentration and matrix local amount, respectively. It is useful to recall that we hereafter account only for the soluble component of the ECM, i.e., for the mixture of long carbohydrate polymers and of non-proteoglycan polysaccharides that is isotropically distributed in the tissue without forming large-scale fibrous structures.

We now turn to describe the evolution of the tumor system by distinguishing cell- and molecular-level dynamics.

Cellular scale. Metabolically active cells are here assumed to (i) undergo random phenotypic transitions, (ii) be subjected to selected migratory stimuli, and (iii) either proliferate or acquire an irreversible necrotic fate. The evolution of their density can be indeed described by means of the following trait-structured partial differential equation (PDE), whose boundary and initial conditions will be specified later on:

$$\frac{\partial a(t, x, y)}{\partial t} = \underbrace{D_a \frac{\partial^2 a(t, x, y)}{\partial y^2}}_{\text{phenotypic variations}} + \underbrace{\frac{\partial}{\partial x}\left[\left(w_1(\rho, n, y) - w_2(M, y)\right) a(t, x, y)\right]}_{\text{movement}} + \underbrace{r(y, O, \rho, n) a(t, x, y)}_{\text{proliferation/necrosis}}. \tag{2}$$

The diffusion operator at the r.h.s. of Eq. (2), with constant coefficient $D_a > 0$, models infinitesimally small phenotypic variations occurring within the tumor mass: they are typically a consequence of random epimutation events due to the non-genetic instability characterizing malignant individuals.

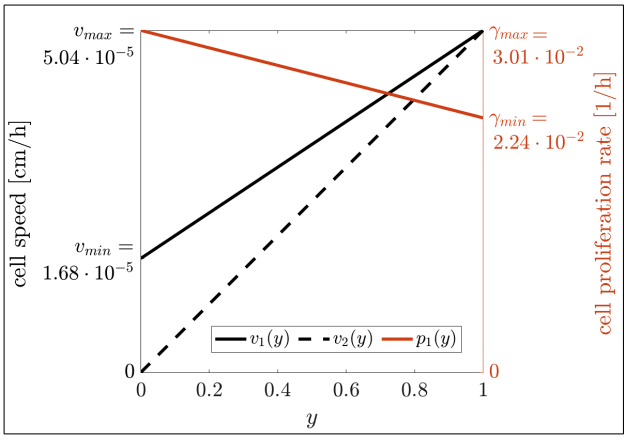

Figure 2: Phenotypic-dependent cell speeds, i.e., $v_1(y)$ and $v_2(y)$, and proliferation rate, i.e., $p_1(y)$. In particular, $v_1(y)$ refers to the pressure-driven velocity term whereas $v_2(y)$ relates to haptotactic dynamics, see Eqs. (3) and (4), respectively. We recall that our model is based on the "Go-or-Grow" hypothesis, which states that cell duplication and migratory potentials are inversely correlated.

The second component at the r.h.s. of Eq. (2) is an *advection velocity*: in our context, it models the response of the different cell clones to selected migratory stimuli. Specifically, this term, that hereafter will be referred to as *cell migration velocity*, is assumed to be due to two contributions: an oncotic (solid) pressure, denoted as w_1, and a haptotatic signal, denoted as w_2. The former results in the cell tendency to spread towards areas with more available space, i.e., with reduced cell density, and can be modeled with a Darcy-type law, see Lorenzi et al. (2017); Perthame et al. (2014):

$$w_1(\rho(t,x), n(t,x), y) = v_1(y)\frac{\partial_x(\rho(t,x)+n(t,x))}{|\partial_x(\rho(t,x)+n(t,x))|}, \tag{3}$$

with $\partial_x := \partial/\partial x$ and $v_1(y) = y(v_{\max} - v_{\min}) + v_{\min}$ (Fig. 2). In particular, Eq. (3) takes into account the fact that also necrotic agents occupy space within the host, therefore increasing the cell mass locally perceived by active cell variants.

The second term w_2 models individual movement towards tissue regions with higher concentrations of ECM elements, as perceived by the probing activity of cell surface receptors (e.g., integrins):

$$w_2(M(t,x), y) = v_2(y)\frac{\partial_x M(t,x)}{|\partial_x M(t,x)|}, \tag{4}$$

with $v_2(y) = y\, v_{\max}$ (Fig. 2). It has not been explicitly demonstrated that haptotaxis occurs in all *in vivo* conditions: however, its relevance in tumor invasion has been largely shown, due to the high responsiveness of malignant cells to gradients of fixed matrix macromolecules.

In Eqs. (3) and (4), cell speed and direction of movement are decoupled, given their distinct physical meaning. The former, quantified by the scalar functions $v_1(y), v_2(y) : Y \mapsto [0, v_{\max}]$, is in fact determined by intrinsic cell determinants (that are implicitly assumed to depend on the phenotype), the latter is instead formally correlated to external factors, such as the pattern of available space and resources. In particular, individuals with the highest migratory potential (i.e., characterized by $y = 1$) move with the maximal speed value $2\, v_{\max}$. On the other hand, individuals characterized by the lowest migratory ability (i.e., identified by $y = 0$) are unable to perceive the matrix distribution and to move accordingly (i.e., $v_2(0) = 0$) but are permitted to crawl towards less crowded areas (i.e., $v_1(0) = v_{\min}$). In fact, cells with a high enough proliferation potential typically inhibit internal pathways involving molecular motors (Rho, Rac) at the basis of *active* movement: therefore, they can only *passively* displace, i.e., pushed by hydrostatic stresses exerted by surrounding individuals (Gaggioli et al. (2007)).

The reaction term in Eq. (2) expresses local variations in the mass of viable cells due to proliferation or necrosis, whose rates are given by the functions p and q, respectively:

$$r(y, O(t,x), \rho(t,x), n(t,x)) = \underbrace{p(y, O(t,x), \rho(t,x), n(t,x))}_{\text{proliferation}} - \underbrace{q(O(t,x))}_{\text{necrosis}}. \tag{5}$$

In particular, the net growth is assumed to depend on (i) individual actual phenotype, (ii) molecular environmental conditions (i.e., oxygen level), and (iii) physical limitations determined by the available space. In this respect, p can be factorized as it follows:

$$p(y, O(t,y), \rho(t,x), n(t,x)) = p_1(y)\, p_2(O(t,x))\, p_3(\rho(t,x), n(t,x)). \tag{6}$$

The duplication law p_1 accounts for the fact that the phenotypic state $y = 0$ corresponds to the cell variant with the highest proliferation rate, say $\gamma_{\max}$, whereas a trait value $y = 1$ is given to the cell clone which poorly undergoes mitotic events, as quantified by the lowest rate $\gamma_{\min}$. To avoid overcomplications, we assign to p_1 a linear trend:

$$p_1(y) = (\gamma_{\min} - \gamma_{\max})y + \gamma_{\max}. \tag{7}$$

We then assume that active cells proliferate proportionally to the quantity of oxygen that exceeds a basal concentration $O_{\min}$, which corresponds to the amount of molecular substance needed to remain viable and to avoid necrotic transition. More specifically, the relation between cell duplication rate and available chemical is given by a classical Michaelis-Menten law, as done in Ardaševa et al. (2020); Lorenzi et al. (2018); Villa et al. (2021); Ward and King (1997):

$$p_2(O(t,x)) = \frac{O(t,x) - O_{\min}}{\alpha_O + (O(t,x) - O_{\min})}\, H(O(t,x) - O_{\min}), \tag{8}$$

being $H(O(t,x) - O_{\min}) = \left\{1\,, \text{ if } O(t,x) \geq O_{\min};\ 0\,, \text{ if } O(t,x) < O_{\min}\right\}$ the Heaviside function. Eq. (8) therefore implies that mitotic events are prohibited in the case of insufficient presence of oxygen.

The factor p_3 in Eq. (6) finally models the fact that the mitotic cycle is typically disrupted in overcompressed cells, although abnormal proliferation is a relevant characteristic of malignant masses. This phenomenon can be replicated by setting the following logistic law:

$$p_3(\rho(t,x), n(t,x)) = 1 - \frac{\rho(t,x) + n(t,x)}{k}, \tag{9}$$

where $k > 0$ is the tissue carrying capacity. In Eq. (9), we consider that the available space is reduced by the presence of both viable and necrotic individuals, coherently to the case of the pressure-driven velocity term ω_1. It is useful to remark that intercellular competition for environmental free areas and resources has an effect on the growth rates p_2 and p_3.

Active cells irreversibly acquire a necrotic fate when they experience a drop in the available oxygen concentration down to the basal level $O_{\min}$. In this respect, the sink term q in Eq. (5) reads as

$$q(O(t,x)) = \eta H(O_{\min} - O(t,x)), \tag{10}$$

where H is again the Heaviside function and η represents a unit transition rate. We are indeed assuming an inevitable relationship between a low enough amount of resources and a disruption of intracellular metabolic activity, which is in common for all viable cell variants.

The same rate $q(O(t,x))$ establishes the growth of the necrotic population as a consequence of the metabolic inactivation of oxygen-deprived cells, i.e.,

$$\frac{\partial n(t,x)}{\partial t} = q(O(t,x))\rho(t,x), \tag{11}$$

ρ being, as seen, the number density of active individuals. Eq. (11) implies that necrotic cells remain freezed in space. This choice is consistent: when an individual becomes necrotic its surface ion pumps cease to function causing intracellular osmosis of water, swelling, and subsequent bursting. The remaining solid volume fraction is then replaced by calcium phosphate and/or calcium oxalate molecules that bind together and form calcite crystals. The process, called *calcification*, finally confers to the necrotic cell full rigidity and incompressibility.

Molecular scale. We assume that oxygen diffuses within the tissue, naturally decays and it is consumed by viable cells (independently from their phenotype). Its kinetics can be therefore described by the following reaction-diffusion (RD) equation:

$$\frac{\partial O(t,x)}{\partial t} = \underbrace{D_{\mathrm{O}}\frac{\partial^2 O}{\partial x^2}(t,x)}_{\text{diffusion}} - \underbrace{\lambda_{\mathrm{O}} O(t,x)}_{\text{natural decay}} - \underbrace{\beta_{\mathrm{O}}\rho(t,x)\,O(t,x)}_{\substack{\text{consumption by}\\ \text{active tumor cells}}}, \tag{12}$$

where D_{O}, λ_{O} and β_{O} are constant coefficients. The use of an average homogeneous and isotropic diffusivity has been proven to be a good approximation, although the chemical successively passes through intracellular fluids, cell membranes and cytoplasmic regions (Tannock (1972); Pogue et al. (2001)). RD equations like Eq. (12) are widely employed in the theoretical literature to describe the kinetics both of oxygen and of other chemicals, see Anderson et al. (2000); Anderson and Quaranta (2008); Trucu et al. (2016); Araujo and McElwain (2004); Bellomo et al. (2008); Bellomo and Preziosi (2000); Cristini and Lowengrub (2010); Moreira and Deutsch (2002); Friedman (2004); Friedman (2007); Eftimie et al. (2011), although they imply an infinite propagation speed. This issue could be in principle prevented by the use of hyperbolic (heat-like) laws (Cattaneo (1952)) and/or by considering a nonlinear degenerated diffusive behavior for the molecular substances of interest, as typically done in the context of porous media (see Vazquez (2012) and references therein). The level of tissue oxygenation at the onset of tumor growth, as well as the possibility and the rate of chemical supply from the pre-existing vasculature, will be given by the initial and the boundary conditions associated to Eq. (12).

The soluble component of the ECM is only assumed to be degraded by active tumor cells at a constant rate, i.e.,

$$\frac{\partial M(t,x)}{\partial t} = \underbrace{-\beta_{\mathrm{M}}\,\rho(t,x)\,M(t,x)}_{\substack{\text{consumption by}\\ \text{active tumor cells}}}. \tag{13}$$

For the sake of completeness, we remark that matrix elements are consumed upon contact with cell-secreted metalloproteinases (MMPs). This family of enzymes does not significantly diffuse away from cell membranes and therefore it is consistent to assume a local degradation. ECM digestion by MMPs increases tumor ability to push into the host tissue not only by forming an haptotactic gradient but also by reducing the mechanical rigidity of the surrounding environment and by creating extra space for migration and infiltration of single aggressive cells. The degraded ECM can eventually release associated growth factors that further fuel tumor growth.

2. Results

2.1. Simulation Details

The spatial domain X represents a linear section of a 0.2 cm-large tissue, i.e., $X = [x_1 = 0, x_2 = 0.2]$ cm. The final observation time, as seen denoted by t_{F}, corresponds to the instant at which at least an infinitesimal fraction of cells reaches one of the two point-borders of X. A longer period of observation would in fact imply the description of phenomena relative to extra-tissue tumor invasion (e.g., intravasation and metastatization), that are beyond the scope of this study.

Eqs. (2) and (11), that establish cell dynamics, are equipped by the following initial conditions, that are in common for all simulation settings (except where explicitly stated):

$$a(0,x,y) = A\ \exp\left(-\frac{(x-x_0)^2}{2\sigma_x^2} - \frac{(y-y_0)^2}{2\sigma_y^2}\right), \quad \text{s.t.} \int_Y a(0,x,y)dy < k, \quad \text{for } x,y \in X \times Y; \tag{14}$$

$$n(0,x) = 0, \quad \text{for } x \in X, \tag{15}$$

with $A > 0$. We are indeed assuming that, at the beginning of all numerical realizations, a node of malignant viable cells is already present within the tissue, with the following characteristics: (i) each cell phenotype has a full Gaussian profile along the spatial dimension, centered at the middle point of the domain (i.e., $x_0 = 0.1$ cm and $\sigma_x = 10^{-3}$ cm) and (ii) the cell mass has a half-normal distribution in the trait space, with peak at $y_0 = 0$ being $\sigma_y = 0.2$ (Fig. 3 (B)). In this respect, at $t = 0$, the overall density ρ of active individuals is symmetrically disposed w.r.t. x_0 (Fig. 3 (A)) and it is mainly composed of proliferative cell variants with only a small fraction of motile agents. At the onset of its growth, the malignancy lacks of a necrotic bulk.

Eq. (2) has zero-flux conditions at the border of the phenotypic domain, i.e., $\partial_y a(\cdot,\cdot,0) = \partial_y a(\cdot,\cdot,1) = 0$. This is consistent with the fact that malignant cells can not be characterized by a trait smaller than 0 or higher than 1. Boundary conditions on the domain X are instead not necessary to the well-posedness of the problem: in all forthcoming simulation settings, the characteristic lines from the spatial axis will constantly point outside the domain, see Salsa (2016) for a more detailed explanation.

Eqs. (12) and (13), that regulate chemical kinetics, are then completed with conditions:

$$O(0,x) = O^0(x), \tag{16}$$

$$M(0,x) = M^0(x), \tag{17}$$

where $O^0(x)$ and $M^0(x)$ define the initial spatial profiles of the molecular substances included in our model. These two functions, as well as the boundary conditions relative to oxygen evolution, will be specified for each simulation setting to account for different biological scenarios.

Parameters estimate. The proposed approach is intrinsically multi-parametric, which would be in principle a limiting factor of its usefulness. However, the majority of model coefficients has a clear and direct biological meaning and therefore a proper estimate has been done taking advantage of the empirical literature. In this respect, we have referred to experimental works dealing with a wide spectrum of diseases which is consistent since we here account for a generic tumor.

The diffusion coefficient of random phenotypic variations, i.e., D_a, has been taken equal to $3.6 \cdot 10^{-10}$ h^{-1}, which is one or two orders of magnitude larger than the rate of somatic DNA mutations, as reported in Doerfler and Böhm (2006); Duesberg et al. (2000) in the context of vascularized tumors. The maximal value of cell speed $v_{\max}$ has been fixed to $5.04 \cdot 10^{-5}$ cm/h, whereas the minimal threshold $v_{\min}$ (which characterizes individual response to oncotic pressures) to $1.68 \cdot 10^{-5}$ cm/h. Under these assumptions, the modulus of the overall cell velocity, which is given by the sum of the intensities of w_1 and w_2, does not exceed the corresponding experimental counterpart evaluated for different malignancies, see Diao et al. (2019); Parker et al. (2018); Staneva et al. (2019). The coefficients $\gamma_{\min}$ and $\gamma_{\max}$ quantify the minimal and maximal ability of cells to proliferate according to their phenotypic state y in the case of a given amount of oxygen and available space. The chosen values $\gamma_{\min} = 2.24 \cdot 10^{-2}$ h^{-1} (i.e. $5.37 \cdot 10^{-1}$ days^{-1}) and $\gamma_{\max} = 3.01 \cdot 10^{-2}$ h^{-1} (i.e. $7.23 \cdot 10^{-1}$ days^{-1}) fall within the range of duplication rates measured by Oraiopoulou and coworkers in the case of different glioblastoma cell lines cultured and grown *in vitro* as spheroids Oraiopoulou et al. (2017). The carrying capacity has been set equal to $k = 10^3$ cells/cm assuming a 10 μm-mean cell diameter, as computationally measured in Shashni et al. (2018). The initial cell configuration is finally set at $A = 10^3$ cells/cm, which results in a disease composed, at its onset, by $N_a(0) = 2$ active individuals. Upon a proper dimensional rescaling and approximation,

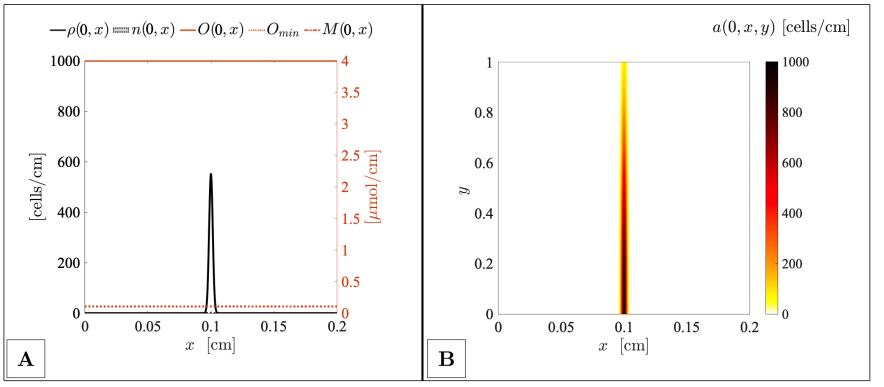

Figure 3: Initial configuration of the tumor microenvironment. (A) The malignant mass initially consists of a bulk of active cells with a spatial Gaussian profile. In the reference case, the host tissue is initially well-oxygenated and characterized by an abundance of soluble matrix elements. (B) The progenitor tumor is mainly formed by cell clones with significant proliferative potential, with a poor presence of more motile variants. At $t = 0$, each cell phenotype has a normal distribution in space. We remark that the initial cell condition, given by Eqs. (14)-(15), is kept fixed for all simulation settings, whereas the profile of the molecular landscape is varied to reproduce different scenarios.

	Parameter	Description	Value [Units]	Reference(s)
cell dynamics:	$D_{\mathbf{a}}$	phenotypic variation rate	$3.6 \cdot 10^{-10}$ [h^{-1}]	Doerfler and Böhm (2006); Duesberg et al. (2000)
	$\gamma_{\mathbf{min}}$	minimal cell duplication rate	$2.24 \cdot 10^{-2}$ [h^{-1}]	Oraiopoulou et al. (2017)
	$\gamma_{\mathbf{max}}$	maximal cell duplication rate	$3.01 \cdot 10^{-2}$ [h^{-1}]	Oraiopoulou et al. (2017)
	$v_{\mathbf{min}}$	minimal cell speed	$1.68 \cdot 10^{-5}$ [cm/h]	Staneva et al. (2019)
	$v_{\mathbf{max}}$	maximal cell speed	$5.04 \cdot 10^{-5}$ [cm/h]	Staneva et al. (2019)
	k	tissue carrying capacity	10^3 [cells/cm]	Shashni et al. (2018)
	η	rate of necrotic transition	$3.6 \cdot 10^3$ [h^{-1}]	model estimate
	A	initial maximal cell density	10^3 [cells/cm]	Benzekry et al. (2014); Spratt et al. (1995)
oxygen kinetics:	$D_{\mathbf{O}}$	oxygen diffusion coefficient	$3.6 \cdot 10^{-2}$ [cm^2/h]	Mueller-Klieser and Sutherland (1984)
	$\lambda_{\mathbf{O}}$	oxygen natural decay rate	$3.6 \cdot 10^{-4}$ [h^{-1}]	Cumsille et al. (2015)
	$\alpha_{\mathbf{O}}$	Michealis-Menten oxygen constant	$1.62 \cdot 10^{-1}$ [μmol/ cm]	Daşu et al. (2003)
	$\beta_{\mathbf{O}}$	oxygen consumption rate	$1.8 \cdot 10^{-1}$ [cm/(cells $\cdot$ h)]	model estimate
	$O_{\mathbf{min}}$	oxygen basal level	$1.06 \cdot 10^{-1}$ [μmol/cm]	Brown and Wilson (2004)
matrix kinetics:	$\beta_{\mathbf{M}}$	ECM consumption rate	$1.8 \cdot 10^{-5}$ [cm/(cells $\cdot$ h)]	model estimate

Table 1
Reference parameter setting.

this value is consistent with the quantity of malignant cells that composed the tumor spheroids injected in mice in the experimental designs proposed in Spratt et al. (1995); Benzekry et al. (2014).

The basal concentration of oxygen O_{min}, that allows cells to remain viable and to duplicate, has been taken equal to $1.06 \cdot 10^{-1}$ μmol/cm, in agreement with the critical threshold leading to anoxia used in Brown and Wilson (2004). The characteristic constant α_{O} of the Michaelis-Menten proliferation law has been fixed to $1.62 \cdot 10^{-1}$ μmol/cm, as reported in Daşu et al. (2003).

The oxygen diffusion coefficient has been taken equal to $D_{\text{O}} = 3.6 \cdot 10^{-2}$ cm^2/h, as reported in Mueller-Klieser and Sutherland (1984). The effective oxygen (rsp., matrix) consumption rate is given by the parameter β_{O} (rsp., β_{M}). In particular, we set β_{O} =$1.8 \cdot 10^{-1}$ cm/(cells $\cdot$ h) and β_{M} =$1.8 \cdot 10^{-5}$ cm/(cells $\cdot$ h), taking into account both of the literature, i.e., Freyer and Sutherland (1983, 1986); Murphy and Gavrilovic (1999); Scianna and Preziosi (2012a,b), and of preliminary simulations. The oxygen decay rate $\lambda_{\text{O}} = 3.6 \cdot 10^{-4}$ h^{-1} has been finally set in accordance with Cumsille et al. (2015). The employed parameters setting is listed in Table 1.

Quantification of model results. The aim of our work is to investigate how environmental conditions and biophysical determinants of cancer cells influence tumor growth. In this respect, we will focus on observables relative both to the *macroscopic* characteristics of the disease and to its *microscopic* features, i.e., internal heterogeneity.

More specifically, the macroscopic morphology of the malignancy will be described in terms of spatial extensions of the active and of the necrotic cell submasses, say d_{a} and d_{n}, respectively, and of the corresponding total number of cells, i.e., N_{a} and N_{n}, respectively. Such two quantifications, taken together, will allow to differentiate large but scattered tumors from concentrated but overdense diseases. Furthermore, d_{a} and d_{n} will be relevant parameters for the evaluation of the invasive potential of the malignant mass. For instance, larger values of the ratio $d_{\mathrm{a}}/d_{\mathrm{n}}$ will characterize more aggressive lesions.

A description of tumor internal composition will be instead obtained by the normalization of the phenotypic distribution of active cells across the whole tissue w.r.t. their total number, i.e., by the quantity

$$F(t,y) = \frac{\int_X a(t,x,y)\,dx}{N_{\mathrm{a}}(t)}. \tag{18}$$

Each value of F will in fact give the percentage of individuals with the y-th trait that are *globally* present within the entire mass at a given time t. Such a quantification will allow to identify the predominant phenotypic variant and therefore to give an indication of the tumor severity grade.

Numerical method. The numerical approach used here is basically the same as those employed in the case of similar models, see Fiandaca et al. (2021) and Lorenzi et al. (2021), where a formal analysis of the computational method is also provided in the Appendix. Specifically, we have solved each equation included in the model with a numerical scheme proper for its structure. In all cases, we have employed uniform grids for the spatial domain X, the phenotypic space Y, and the time interval T, with sufficiently small discretization steps, i.e., $\Delta x = 1.33 \cdot 10^{-4}$ cm, $\Delta y = 0.01$, and $\Delta t = 2.4 \cdot 10^{-3}$ hours, respectively. For instance, Eq. (2) has been solved employing a classical time-split method. In particular, we have opted for a forward upwind scheme for the transport terms and for an explicit finite-difference scheme to approximate the diffusion term in y with a three-point stencil. An implicit-explicit finite-difference scheme has been instead employed for the reaction term, as also suggested in LeVeque (2007). Eq. (12) has been solved with a $\Theta-$method, being $\Theta = \frac{1}{2}$. In particular, the diffusion term has been computed using an explicit centered finite-difference scheme. Finally, we have employed an explicit Euler method for Eqs. (11) and (13). All numerical computations have been performed in MATLAB®.

2.2. Reference Simulation

In the first simulation setting, hereafter referred to as the *reference* one, we describe tumor growth in an oxygenated tissue. Specifically, we assume the presence of a functional blood vessel at each end point of the domain. Dirichlet boundary conditions $O(t,0) = O(t,10) = \overline{O} = 4$ μmol/cm, for all $t \in T$, are indeed set to implement a constant oxygen supply from the supposed vasculature. A basal chemical concentration $O^0(x) = \overline{O}$ is initially present within the entire tissue (i.e., for all $x \in X$) to account for preexisting small fonts of oxygen (e.g., capillaries) that will undergo degradation as a consequence of the expansion of the malignant mass. This is of course a simplification, since oxygen punctual sources distributed along the entire domain may better reproduce micro-vascular patterns. The extracellular matrix is set to have a constant initial profile as well, being $M^0(x) = \overline{M} = 4$ μmol/cm for all $x \in [0, 0.2]$ cm. The progenitor disease consists of a node of active cells located at the center of the tissue, as defined in Eq. (14). Such an initial system configuration is reproduced in Fig. 3.

The early stages of tumor growth are characterized by a spatial expansion of the malignant mass (cf. Figs. 3 (A) and 4 (A)), accompanied by a transient reduction in the peak of its density (from 600 to nearly 500 cells/cm). Cell clones with higher migratory capacity (identified by higher values of y) start in fact to radially spread away (each variant at its characteristic speed) stimulated by pressure effects and by the abundance of available matrix components (cf. Figs. 3 (B) and 4 (B)). Such a mass dispersion is not immediately balanced by duplication events occurring to highly mitotic cell phenotypes. However, cell proliferation quickly prevails leading to the increment in the overall density of malignant individuals with a peak of almost 800 cells/cm (cf. Fig. 3 (C)).

During the above-described dynamics, the mass maintains a Gaussian-like profile: in particular, its core is a dense region populated by least aggressive cells, while its tails are sparse areas populated by cells with more aggressive traits (Fig. 4 (D)). Such cell-level dynamics have a feedback/feedforward effect on the molecular scale. In fact, substantial

consumption both of oxygen and of matrix components occurs at the tissue areas occupied by the disease, with local decrements obviously determined by the local amount of malignant individuals (we remark that the oxygen profile is smoother than the ECM one due to its diffusive behavior).

At $t = t_n = 14$ days, the level of oxygen at the inner part of the mass drops down to the critical value O_{min} necessary to maintain cell viability. As a consequence, a bulk of tumor cells (characterized by negligible motility) experiences hypoxia and therefore undergoes the irreversible necrotic transition (Fig. 4 (C-D)).

The subsequent phases of tumor development (i.e., for $t > t_n$) are characterized by two simultaneous processes. On one hand, further consumption of oxygen results in a gradual enlargement of the necrotic core, which involves cells not able to move towards domain areas with more favorable environmental conditions. On the other hand, the external regions of the disease go on expanding and invading the host, driven by motile cell clones which are able to escape hypoxia (Fig. 4 (E-F)).

It is useful to underline that (i) the molecular landscape does no longer vary in the portion of the tissue occupied by the necrotic bulk of the cancer mass, since the component cells are completely deprived of any activity, and (ii) the peak of the density of active cells grows up to nearly 920 cells/cm.

At the end of the observation time (i.e., at $t = t_F = 22$ days), the tumor has actually infiltrated the entire host, which is indeed severely compromised (Fig. 4 (G-H)). In particular, the malignant mass has maintained its bi-compartmental characteristic: it is in fact formed by an internal necrotic core and by two symmetric peripheries composed by metabolically active individuals, whose density drops in space moving away from the tumor center. In particular, in each of these two regions, less motile cell variants are selected at the more internal area whereas more motile cell phenotypes occupy the external edge. Such a spatial heterogeneity has been consistent for the entire system evolution. In particular, fronts composed of fully motile cells have reached the vessels located at the domain borders. As explained in the Introduction, these individuals represent the most dangerous portion of the disease, since they may enter the host bloodstream and start the metastatic cascades, i.e., extravasate at a distant site and establish secondary colonies with devastating consequences for the wellbeing of the patient. Such subpopulations are barely detected also in the case of surgical resection of the main tumor body, therefore increasing the possibility of recurrences.

The progression of our virtual malignancy, as well as the specific spatial distribution of the different cell phenotypes, recapitulates previous experimental evidence dealing with a large spectrum of solid tumors. It is the case of malignant spheroids of ovarian carcinomas grown in spinner cultures (Burleson et al. (2006); Shield et al. (2009)) or breast (Gatenby et al. (2007)). Moreover, our model results are consistent with the development of avascular gliomas: they in fact show an area of central necrosis surrounded by a rim of viable cells, see Giese et al. (2003) and references therein. Further, measurements on the expression of the Ki-67protein have demonstrated that cells within the core of this type of tumor possess higher proliferative activity compared to those located at the invasive edges (Stein et al. (2007)). Analogous evidence emerges from the analysis of the progress of glioblastomas both embedded *in vitro* in collagen gels (Khaitan et al. (2006)) and implanted in mice (Abramovitch et al. (1995); Castro et al. (2003)). Close to our outcomes, mesenchymal cancer stem cells have been found to be abundant near the tumor-stroma boundary (i.e., at the external region of the malignant mass) while cancer stem cells exhibiting a hybrid epithelial/mesenchymal phenotype tend to localize in the interior of the tumor (Liu et al. (2014)). Similar growth of primary solid tumors, in terms both of the overall mass evolution and of the internal composition, has been also predicted by different types of theoretical models, see the reviews Araujo and McElwain (2004); Bellomo et al. (2008); Byrne et al. (2006); Chaplain (1996); Quaranta et al. (2005), and the comprehensive books Cristini and Lowengrub (2010); Preziosi (2003).

The evolution of the molecular landscape within the host and across the malignant mass agrees with experimental and numerical outcomes as well. For instance, in Grimes et al. (2014), the authors have predicted similar trends for the oxygen profile in multicellular tumor spheroids, using an analytical solution of a spherical reaction–diffusion equation. In fact, their method analytically shows higher chemical consumption at the inner and dense area of the mass and lower chemical consumption at the external and less populated rim. They have also demonstrated how the extension of hypoxic and normoxic regions depends on the overall spheroid size. Their theoretical data have been supported by empirical measurements relative to stained sections of human colorectal carcinoma spheroids.

For simplicity, we hereafter distinguish two different temporal phases of the simulated tumor growth, separated by t_n, i.e., by the time instant at which a necrotic fraction of cells appears within the malignant mass: $T_1 = [0, t_n]$ and $T_2 = (t_n, t_F]$. Of course, $T = T_1 \cup T_2$. In this respect, the morphological analysis in Fig. 5 (A) shows that the extension of the mass of active cells (d_a) almost linearly increases during the entire period of observation. In particular, it expands significantly fast until the onset of the necrotic core to reach a value of $d_a(t_n) \approx 0.12$ cm and then it moderates its growth rate. It is useful to underline that, for $t > t_n$, d_a is calculated as the overall tumor diameter minus the extension

of the necrotic region (d_n). At the end of the observation time, the viable tumor mass has damaged nearly 0.15 cm of tissue. On the other hand, the total number of active individuals (N_a) is characterized by an exponential growth during the period T_1, followed by a quasi-linear trend in T_2, with $N_a(t_F) \approx 93$ cells. After its appearance (i.e., for $t > t_n$), the necrotic bulk linearly enlarges at almost the same rate of the active mass to reach a final extension close to 0.05 cm. The amount of its component cells instead increases more rapidly than the corresponding quantity of viable individuals in the same time-period.

To facilitate a quantitative comparison of the different simulation settings, we hereafter estimate the growth rates of the number of active cells in each of the two phases T_1 and T_2. More specifically, $r^{\exp}_{T_1}$ (rsp., $r^{\text{lin}}_{T_2}$) indicates the coefficient of the exponential (rsp., linear) function that best fits the evolution of N_a in the time interval T_1 (rsp., T_2). In this reference case, we obtain $r^{\exp}_{T_1} \approx 0.29$ days^{-1} and $r^{\text{lin}}_{T_2} \approx 2.51$ cells/days.

A two-step growth (i.e., from-exponential-to-linear) has been proven to characterize a wide spectrum of tumors from the early 70s (Folkman and Hochberg (1973)). For instance, in Benzekry et al. (2014), the authors have shown that such a characteristic growth profile is able to reproduce more accurately than others experimental data relative to volume extensions of orthotopic human xenograft breast carcinomas, implanted in mice. A quasi-exponential expansion in the absence of necrosis has been also observed in the case of spheroids formed by glioblastoma cell lines with different proliferation potentials and cultured *in vitro*: in particular, they reach an ≈ 1 mm^2-area in nearly two weeks, i.e., a dimension that is consistent to our simulation results Oraiopoulou et al. (2017). Interestingly, the same authors have reproduced the same growth dynamics with a hybrid discrete-continuous mathematical approach.

We remark that our reference case does not give Gompertz-like kinetics, where critical quantities such as volume or cell number have instead a sigmoid profile with an asymptotic convergence to a maximal threshold value. This is probably due to the fact that Gompertzian laws have been observed in cases of malignant masses that grow in tissues where critical nutrients are consumed and not further supplied, or, in cases in which the carrying capacity of the tissue is reached. Neither of the two phenomena takes place in our reference setting.

The time evolution of the *global* fraction of the active cell variants shown in Fig. 5 (B) reveals that, in the T_1 phase, low aggressive cells are the predominant clones. In the subsequent phase T_2, we can instead observe the progressive disappearance of cell variants with substantially high proliferation potentials (i.e., those with trait lower than 0.3): given their poor migratory capacity, they are in fact unable to move from the tissue areas deprived of oxygen and therefore undergo necrosis. The result is a gradual but constant phenotypic shift of the disease towards more motile cell phenotypes: at the end of the observation time, the predominant cell clone has indeed a trait value y close to 1.

Evolutionary selection of more motile cell clones in the case of harsh tissue conditions (and *vice versa*) have been found out in Hatzikirou et al. (2012) with a lattice gas cellular automaton (LGCA) based on the "Go-or-Grow" mechanism and supported by a number of experimental evidence on glioblastomas. In particular, Hatzikirou and coworkers have demonstrated that increments in oxygen supply in the tumor microenvironment lead to increments in the fraction of proliferative cell clones and to simultaneous decrements of the fraction of more aggressive (i.e., motile) variants.

2.3. Tumor growth upon variations in cell determinants or environmental conditions

In the previous section, we have shown the ability of our model to reproduce several aspects of the growth of a generic tumor within an oxygenated tissue, also characterized by an (initial) abundance of matrix elements.

We now turn to a predictive perspective and analyze the progression of the disease in the case of

- manipulations of specific biophysical characteristics of viable malignant cells, with the aim to find out possible relations between individual cell behavior and collective multicellular dynamics;
- variations in the chemical landscape of the host tissue. Microenvironmental conditions have been in fact widely shown to play a significant role in tumor invasive potential, for instance, affecting cell molecular and physical state and inducing clonal diversity (Enam and Klaus (1998); Höckel et al. (1996)).

In other words, we are going to shed light on how the evolution of the malignancy is influenced by modifications of either internal or external determinants. The proposed results will be then reviewed from a therapeutic point of view in the conclusive section of the work.

2.3.1. Investigation of the impact of cell determinants variations

Inhibition of haptotaxis. We first neglect cell migratory response to ECM gradients by setting $w_2 = 0$ in Eq. (2). From a biological perspective, this mimics an inhibited activity of integrins that, as seen, are able to sense the presence of

matrix elements and to stimulate cell behavior according to their amount and distribution. The movement of all viable cell phenotypes is indeed only due to oncotic pressure.

In the early stages of growth (i.e., before the onset of necrosis), the malignant mass is characterized by a slower spatial extension and an higher density of viable cells w.r.t. the reference setting (cf. Figs 4 (A-B) and 6 (A)). For instance, the peak of the Gaussian profile of ρ (after an initial transitory decrement) reaches a value of nearly 850 cells/cm, which will slightly increase over time. A further quantification of this phenomenology is given by the fact that, in this case, we have $d_{\mathrm{a}}(t_n = 20\,\mathrm{days}) = 0.1$ cm whereas, in the case of the reference simulation, the lesion already extended for nearly 0.12 cm at $t = t_{\mathrm{n}} = 14$ days (cf. Figs. 5 (A) and 6 (C)).

The underlying rationale is that more aggressive cell variants, having a reduced migratory potential, are no longer able to deeply and quickly invade the host. Rather, they remain close to the bulk of the mass therefore increasing the local cell amount. Coherently, we observe an enhanced phenotypic heterogeneity across the tumor: each volume fraction of the disease is in fact characterized by the coexistence of a wide range of active cell clones (Fig. 6 (D)). However, the core of the tumor is still populated by highly mitotic variants whereas more aggressive individuals are located at its external regions.

As already sketched, the necrotic core here emerges at $t_{\mathrm{n}} \approx 20$ days, i.e., almost one week later than in the reference setting. This is due to the fact that the oxygen concentration at the core of the tumor decreases more slowly than in the reference case. The chemical is, in fact, efficiently supplied by diffusion from the rest of the domain, where its level does not undergo significant consumption as a consequence of the localized growth of the malignant mass.

The later phases of tumor development amount in a rapid enlargement of the necrotic bulk, accompanied by a slow invasion of the host by the two viable lateral masses (Fig. 6 (B)). Coherently to our previous observations, they have a higher degree of heterogeneity w.r.t. the reference case, being characterized by the local presence of several cell variants. However, more proliferative cells still populate their internal regions whereas more motile individuals are predominant at their external edges (Fig. 6 (E)). The most aggressive cell clones finally reach the vasculature at $t_{\mathrm{F}} \approx 41$ days, i.e., almost 3 weeks later than in the reference setting. At the end of the observation period, the necrotic area of the tumor occupies a substantially large portion of the disease (Fig. 6 (B)).

By comparing the plots relative to tumor morphological quantities in Figs. 5 (A) and 6 (C), we can observe that the total number of active individuals has again an exponential growth during the first phase T_1 (with $r_{T_1}^{\mathrm{exp}} \approx 0.19\,\mathrm{days}^{-1}$), followed by a poor increment in the second phase T_2 to finally reach a value of approximately 102 cells, which is however 10% higher than the corresponding threshold in the reference case. The extension d_{a} of the mass of viable cells instead maintains a quasi-linear increment for the entire period of observation, whose rate however decreases after t_{n}. As already observed, the part of the tissue invaded by the active part of the tumor at the end of the simulation is smaller than in the previous case, as $d_{\mathrm{a}}(t_{\mathrm{F}}) \approx 0.135$ cm. The necrotic bulk, in turn, linearly grows more rapidly than the mass of active cells, in term both of spatial extension and of cell number, to reach final values close to 0.065 cm and 56 cells, respectively. These quantities are substantially higher than their counterparts obtained in the reference case.

Observing the time evolution of F in Fig. 6 (F), we can notice that a phenotypic shift towards more aggressive cell variants again occurs as a consequence of necrosis. In this case, such an irreversible transition involves a wider spectrum of cell clones (i.e., those defined by a trait ranging from 0 to approximately 0.5). This is due to the fact that all cells have reduced migratory stimuli and therefore a large number of variants is not able to escape hypoxia. The globally predominant cell phenotype at the end of the observation time is again the pure motile one (i.e., the one characterized by $y = 1$).

The proposed results have clearly stated the relevance of haptotaxis as a driving-mechanism for tumor invasion.

Similar numerical outcomes could be also obtained setting $\beta_{\mathrm{M}} = 0$, which corresponds to an inhibition of MMP activity. Such a model manipulation in fact would imply a constant matrix profile along the entire period of observation. This, in turn, would cause the absence of haptotaxis stimuli, which rather rely on ECM spatial inhomogeneities (cf. Eq. (4)). In this respect, experimental evidence has shown the correlation between the metastatization ability of most malignancies and the secretion of matrix degrading enzymes, see for instance Friedl and Wolf (2003); Kenny et al. (2008) and references therein. Disruption of haptotactic mechanisms can be obtained *in vitro* also by adding saturating amounts of matrix components, that extinguish substrate inhomogeneities: cells cultured in ECM with high enough collagen densities have been in fact demonstrated to undergo a dramatic down-regulation of their migratory capacity, driven by the fact that their integrin receptors are completely engaged (Engler et al. (2004); Gaudet et al. (2003)). This aspect may be accounted in our approach by relating the haptotactic speed not only to the cell phenotype but also to the local amount of matrix elements, i.e., by setting $v_2 = v_2(y, \boldsymbol{M}(t, x))$.

We underline that reduction in cell migratory potential may also derive by neglecting the pressure-driven term w_1 in Eq. (2). From a biological perspective, this model setting would reproduce the case of tumor cells with hyper deformability and compressibility, i.e. that are not subjected to pressure stresses from neighbouring individuals since they are able to completely adapt their body to the surrounding cell configuration. However, this would be an implausible scenario: although cell cytoplasmic region is almost fluid, intracellular organelles such as the nucleus are in fact voluminous and sufficiently stiff to represent limiting factors for dramatic cell squeezing and shrinking, as widely shown in the experimental literature (Ilina et al. (2011); Irimia and Toner (2009); Wolf et al. (2003)).

Increment in cell proliferation potential. We now enhance cell mitotic potential by increasing of one order of magnitude the value of $\gamma_{\max}$ in Eq. (7) ($\gamma_{\min}$ is instead kept fixed). This implies that all cell variants (those with $y = 1$ excluded) are able to undergo a larger number of mitotic events with respect to the reference case within the same period. In other words, they have a reduced duration of the mitotic cycle.

Before necrosis occurs, the tumor is an overdense mass with unaltered invasive ability (cf. Figs. 4 (A-C) and 7 (A)). In particular, the viable cell fraction maintains a Gaussian-like profile, whose peak reaches almost 1000 cells/cm (i.e., the carrying capacity of the tissue), a threshold subsequently maintained over time. The internal segregation of phenotypes is again characterized by the presence of more aggressive individuals at the tails and less invasive ones at the bulk. However, all cell clones have an increased number of component cells (cf. Figs. 4 (B-D) and 7 (D)). As a result, the environmental oxygen is consumed quickly enough to make almost impossible its supply from the rest of the host. The necrotic transition indeed starts at $t_{\mathrm{n}} \approx 9$ days, i.e., almost 5 days earlier than in the reference setting (Fig. 7 (A)).

The late phases of tumor progression amount in a rapid enlargement of the necrotic core and in a simultaneous invasion of the normal tissue by the remaining (densely populated) active submasses (Fig. 7 (B)). In particular, the two lateral regions of the disease are highly heterogeneous, since each of their volume fractions is characterized by the presence of a large spectrum of viable cell phenotypes, among the survived ones (Fig. 7 (E)).

The most aggressive variants reach the vasculature at $t_{\mathrm{F}} \approx 22$ days, i.e., in the same time-lapse observed in the reference case. This is due to the fact that the spatial evolution of the tumor is driven by both the haptotatic and the pressure driven mechanisms that have been kept unaltered. The necrotic bulk finally occupies a substantially large portion of the disease (Fig. 7 (B)).

In such a hyperproliferative regime, the number of active individuals has a two-step growth as in the previous cases, but with a different fashion. A huge linear increment of viable cells occurs before the onset of necrosis (i.e., $r_{T_1}^{\mathrm{lin}} \approx 7.7$ cells/days) and it is followed by a more moderate grow during T_2, that leads to $N_{\mathrm{a}}(t_{\mathrm{F}}) \approx 106$ (Fig. 7 (C)). The same graph also shows that the extension d_{a} of the mass of viable cells has instead a quasi-linear increment for the entire period of observation, whose rate decreases after t_{n}. The final value $d_{\mathrm{a}}(t_{\mathrm{F}}) = 0.13$ cm is a definitive confirmation of the lower survival potential of the active tumor fraction w.r.t. the reference case. Coherently, the necrotic bulk linearly grows more rapidly than the viable portion of the malignancy, in terms of both spatial expansion and number of component agents, that reach final values of approximately 0.07 cm and 60 individuals, respectively.

We can finally conclude that the necrotic conversion involves, w.r.t. the reference setting, a larger range of cell variants, i.e., those defined by a trait ranging from 0 to approximately 0.4 (Fig. 7 (F)). The underlying reason is that the huge increment in cell density, due to the enhanced proliferation, leads to a significant competition for the available oxygen, that obviously favors cell clones with an high enough migratory potential. The predominant cell variant at the end of the observation time is the one characterized by $y = 0.8$.

Increment in mutation events. We end this subsection by dealing with a tumor characterized by an enhanced possibility of mutations. In this respect, we increase the parameter D_{a} in Eq. (2) of four orders of magnitude. This implies a larger rate of cell phenotypic variations across the malignant mass during the observation period.

From a macroscopic point of view, the resulting dynamics are close to those observed in the reference simulation (cf. Figs. 4 and 8 (A-B)). The overall distribution of viable cells has in fact the same spatio-temporal evolution, in terms of profile, peak, and invasive rate. The necrotic bulk again emerges after nearly two weeks, whereas the tissue is completely compromised almost one week later, i.e., at $t_{\mathrm{F}} \approx 22$ days.

The similarity between this case and the reference setting is clearly confirmed by the graph relative to the morphological determinants: the growth rates of both the viable and the necrotic portion of the tumor are in fact not affected by the increment in the mutation diffusivity (cf. Figs. 5 (A) and 8 (C)).

Differences instead occur at the microscopic scale, i.e., in terms of tumor heterogeneity. In fact, during the entire system evolution, we observe the local coexistence of a larger range of cell phenotypes w.r.t. the reference case (cf.

Figs. 4 and 8 (D-E)). In other words, each cell variant is more diffused across the mass. However, the tendency to have motile clones at the more external regions of the disease and proliferant phenotypes at its more internal areas is preserved. The trait identifying the predominant cell variant at the end of the observation period is $y \approx 1$, as in the reference case (Fig. 8 (F)). However, the percentage of its presence within the mass is lower, which is a further indication of a highly heterogeneous disease. From the same graph, we can finally observe that necrosis again cause the disappearance of cell clones with trait lower than 0.3.

Summing up, we can conclude that the invasive behavior of the malignant mass remains the same despite differences in the spatial distribution of active cell variants: it in fact mainly relies on the presence of at least a fraction of highly aggressive cells (i.e., those defined by $y = 1$) which are able to migrate across the tissue and reach the vasculature to initiate the metastatic cascade.

In our model, we are assuming that epigenetic mutations occurs at a regular rate, quantified by D_a. This is an obvious simplification since each mechanism resulting in a phenotypic alteration is characterized by a distinct probability to occur. Further, we have to admit that our results are in partial disagreement with the cancer literature. In fact, several experimental evidence has shown that tumors with extremely high rates of mutation (even of genetic nature) may have a better prognosis than those characterized by moderate rates, see Maley et al. (2017) and references therein. As commented by Maley and colleagues, high levels of genomic instability may in fact cause the loss of adaptive information in the passage between progenitor and daughter cells. High rates of mutations of single nucleotide variants increase also the possibility of deleterious phenotypic alterations that may lead to an environmental fitness decline and eventually a regression of the overall disease (McFarland et al. (2014, 2013)).

Tumor masses with phenotypic homogeneity. The cooperative behavior of cells with different traits significantly contributes to a successful growth of a malignant mass. Highly motile individuals in fact determine the depth of invasion of the tumor, whereas highly proliferating ones are fundamental in establishing its volume dimensions. In this respect, we now investigate how a strictly homogeneous disease, i.e., composed of a unique cell clone, evolves. In particular, we focus on the cases of a tumor formed for the entire observation time either by cells with the maximal migratory capacity (with trait $y = 1$) or by cells with the maximal proliferation potential (with trait $y = 0$).

In mathematical terms, such scenarios are obtained by setting $y_0 = 1$ (rsp., $y_0 = 0$) in Eq. (14), with a negligible variance $\sigma_y \approx 0$. We also neglect the diffusion term on the phenotypic space in Eq. (2) by fixing $D_a = 0$: this is to avoid the emergence of further cell subpopulations during the evolution of the system. All the other parameters and environmental conditions are kept unchanged w.r.t. the reference case.

As shown in Fig. 9 (top panels), a tumor entirely composed of highly motile cells is characterized by the same temporal dynamics observed in the case of a "normal" heterogeneous mass. In fact, necrosis begins again at $t_n = 14$ days, while the host tissue is completely invaded one week later. A significant difference w.r.t. the reference scenario relies in the fact that the necrotic part of the disease is substantially smaller in terms of both spatial extension and number of component cells. (i.e., $d_n(t_F) = 0.04$ cm and $N_n(t_F) = 24$). This is due to the fact that all malignant cells are here characterized by a relevant migratory capacity and therefore only few of them are not able to escape hypoxia.

A malignant mass entirely composed of only cells with the maximal mitotic potential undergoes a completely different evolution, as expected. In particular, in the early stages, it substantially grows in density (to reach almost the carrying capacity of the tissue) but not in diameter. In this respect, oxygen is only consumed around the center of the domain: such a local decrement is supplied by the diffusion of the chemical from the side areas, thereby delaying the onset of the necrotic transition (i.e., $t_n = 34$ days), see Fig. 9 (D). In the subsequent phases, the tumor goes on invading the host significantly slowly, as the cells located at the external regions of the disease move only upon pressure stresses (i.e., haptotactic signals do not influence cells with $y = 0$). The tissue is finally compromised only after 11 weeks (Fig. 9 (E)). In the contrast with the reference scenario, the final configuration of the tumor here amounts in a larger and overdense necrotic region (i.e., $d_n(t_F) = 0.08$ cm and $N_n(t_F) = 67$), whereas the remaining viable part is smaller but obviously composed of more cells. (i.e., $d_a(t_F) = 0.12$ cm and $N_a(t_F) = 107$), cf., Fig. 9 (F) and Fig. 5 (A).

Our model results are in a good qualitative agreement with the empirical evidence presented in Carey et al. (2013). Therein, the authors show that spheroids composed of breast cells with epithelial characteristics rapidly become dense but have a poor spatial extension; on the opposite, spheroids composed of aggressive, highly motile, breast adenocarcinoma individuals exhibit scarce compactness but definitively larger surface area.

2.3.2. Manipulations of environmental conditions

Absence of functional vasculature. We now analyze how an inadequate environmental vascularization affects the evolution of the disease. In this respect, we first disrupt entirely oxygen supply by completing Eq. (12) with zero-flux

boundary conditions, i.e., $\partial_x O(t,0) = \partial_x O(t,0.2) = 0$, for all $t \in T$. Such a model setting reflects the situation of a host tissue with a basal level of nutrients but characterized by absent or inefficient (due to blood clots or thrombus) preexisting vasculature and by impermeable edges. The rest of model assumptions and parameters are kept unaltered w.r.t. the reference case.

In the proposed scenario, the oxygen is quickly consumed by the malignant mass, being no longer supplied by the host. As a consequence, the necrotic transition begins dramatically early, i.e., at $t_n = 30$ minutes, and it is completed after less than 5 hours (Fig. 10 (A-B)). In this respect, at the end of the observation time, the tumor consists of a metabolically death cluster of individuals, which can be in principle removed for the sake of patient's health. None of the different cell clones has obviously survived.

Given these results, we then wonder on tumor ability to regenerate if the disruption of vascular perfusion mechanisms is only temporary (i.e., a situation denoted as *acute hypoxia* in Bayer and Vaupel (2012)). The fluctuation of oxygen supply is obtained by setting the following, time-variable, boundary conditions: $\partial_x O(t,0) = \partial_x O(t,0.2) = 0$, for $t \in T_{\text{hyp}}$, and $O(t,0) = O(t,0.2) = \overline{O}$, for $t \in T \setminus T_{\text{hyp}}$. The time interval T_{hyp} is set to start at 2 days and to last nearly 1 hour and 20 minute. The rest of model assumptions and parameters are instead kept unchanged w.r.t. the reference case.

As shown in Fig. 11, the malignant mass normally grows until the inhibition of vascular activity. Then, a quick necrosis involves almost the entire disease. However, when oxygen supply is permitted again, the remaining viable part of the tumor takes advantage of the restored normoxic conditions and starts to evolve almost as in the reference case, with the "normal" (long-lasting) necrotic process initiating at $t_n = 16$ days.

More specifically, the tumor invades the entire tissue in almost 3 weeks and its final configuration, in terms of dimensions, number of components cells, and internal phenotypic heterogeneity is close to the one obtained in the reference simulation (cf. Fig. 11 and Fig. 5). In this respect, we can affirm that, in our model, a temporary inhibition of vascular oxygenation has a small effect on tumor dynamics, at least if vascular activity is restored before the complete necrosis of the malignant tissue.

We now assume the presence of a functional blood vessel only at the left side of the tissue. The right edge of the host is instead hypothesized to be impermeable to chemical factors. In mathematical terms, this domain configuration can be obtained by completing Eq. (12) with a Dirichlet condition at the left boundary, i.e., $O(t,0) = \bar{O}$, for all $t \in T$, and a Neumann zero-flux one at the right point edge, i.e., $\partial_x O(t,0.2) = 0$, for all $t \in T$. The rest of the simulation setup is the same as the reference case.

The resulting tumor progression is asymmetric. The left portion of the malignant mass in fact grows as in the reference scenario whereas its right portion evolves as in the case of disrupted oxygen supply (Fig. 12). In particular, necrosis initiates at $t_n \approx 9$ days, i.e., an intermediate time w.r.t. the two previous numerical settings (Fig. 12 (A-C)). This is due to the fact that the oxygen level at the right part of the tissue decreases more slowly than in the case of complete absence of vasculature due to the diffusion of the chemical from the left subdomain, which has instead a nutrient source. At the end of the observation period, the left region of the host is completely compromised by a viable fraction of tumor, whereas the right side is partially occupied by necrotic mass (Fig. 12 (B-D)).

Inhomogeneity in the initial matrix profile. In most tissues, structural ECMs are far from being spatially homogeneous elements. In this respect, we here consider an hypothetical host initially characterized by a (large) region of high matrix density and a (small) region almost deprived of ECM. In particular, the initial matrix profile is defined by the following step-like function:

$$M^0(x) = -\frac{4}{\pi}\arctan(10^5(x - 0.15)) + 2, \text{ for } x \in [0, 0.2]. \tag{19}$$

A drop in the amount of matrix elements is indeed located around the domain point $x = 0.15$ cm (Fig. 13 (A)). The initial tumor configuration and the level of oxygen (which is again supplied by functional vessels present at both domain edges) as well as the values of the model parameters are instead kept unaltered w.r.t. the reference simulation.

Matrix initial inhomogeneity results in an asymmetric progression of the malignancy. In particular, the left part of the mass, located in the portion of the tissue at the left side of the mid point $x = 0.1$ cm, evolves exactly as in the reference case. On the other hand, the right part of the tumor grows as usual until $t = 12$ days, i.e., until its external highly motile edge reaches the point of the host where the ECM density drops: then, it remains almost frozen and no longer invades the tissue (Fig. 13 (D)).

The underlying reason is that cell variants located at the right invasive border of the disease experience a negative matrix gradient that results in a haptotactic velocity that points towards the center of the domain. Such a stimulus is counterbalanced by the pressure-driven velocity term (that instead maintains its outwards direction). In particular, since $v_1(y = 1) = v_2(y = 1)$, cf. Eqs. (3) and (4), purely motile cells completely stop; the other cell clones instead slightly displace rightwards, since $v_1(y) - v_2(y) > 0$ for all $0 \leq y < 1$, causing an accumulation of malignant individuals at the tumor border close to the critical domain point $x = 0.15$ cm.

The necrotic core emerges almost at the same time instant than in the reference simulation, enlarging almost at the same rate; however, its profile accounts for the increased cell density at the right part of the mass (Fig. 13 (E-F)). The invasive behavior of the malignancy, as well as the final observation time, is obviously dictated by the evolution of its left portion (Fig. 13 (F)).

Such specific dynamics impacts on the evolution both of macroscopic and of microscopic tumor observables. For instance, during the first phase T_1, the active mass expands more slowly than in the reference case to settle to a value of $d_a(t_n) = 0.11$ cm (Fig. 13 (B)). This is due to the fact that the right edge of the tumor almost stops invasion at 12 days, i.e., when its front reaches the valley of ECM density. After the onset of necrosis, only the left part of the disease goes on extending: however, its progression is balanced by the enlargement of the necrotic region so that the overall extension of the viable part of the tumor remains almost stable (Fig. 13 (B)). The number of active cells instead evolves quite similarly, in terms of growth rate and final value, to the reference case (cf. Figs. 5 (A) and 13 (B)). This is indicative of the fact that the tumor is formed by the same number of individuals, that are however differently distributed.

In the left part of the tumor, the spatio-temporal evolution of the different viable cell phenotypes remains almost unaltered w.r.t. the reference case. In particular, cell clones with trait lower than 0.3 disappear and the predominant variant at final observation time t_F is given by $y \approx 1$ (Fig. 13 (C)). On the opposite, the right region of the disease is composed of the full spectrum of cell phenotypes (Fig. 13 (G-H-I)). This is due to the above-observed fact that, at the right invasive front, purely motile individuals (that are almost frozen) coexist with cell variants with lower motility that have however moved outwards from the center of the mass upon pressure stresses.

The particular choice of the initial ECM profile is perhaps somewhat exaggerated and unrealistic but it has been employed to emphasize the importance of the matrix pattern (and the resulting density gradients) on aiding or hindering migration of highly aggressive cell variants, that have the potential to metastatisize. Qualitatively similar numerical results would have been produced by other initial distributions of soluble matrix elements.

3. Conclusions

The proposed model has aimed to study the growth of an avascular tumor and the evolution of its internal heterogeneity. In particular, we focus on how its aggressiveness is influenced by intrinsic and extrinsic factors, the former including biophysical manipulations of the neoplastic cells, the latter including variations of the microenvironment surrounding the tumor mass.

Entering in more details, our virtual tumor has been differentiated in viable and necrotic cell fractions, both described by density variables. The active submass has been then structured w.r.t. a continuous trait that has identified cell variants with distinct motility and proliferation rate. In this respect, we have built our approach on the "Go-or-Grow" hypothesis which, as seen, states an inverse correlation between cell migratory capacity and duplication potential. Tumor dynamics have been then set to affect and be affected by molecular key players, i.e., oxygen and matrix elements. The overall model has indeed amounted in a system of (coupled) nonlinear partial differential equations, governing the evolution of the cancer mass and of the chemical substrates.

To quantify our results, and to facilitate comparison between different scenarios, we have evaluated tumor observables relative to macroscopic and microscopic characteristics of the disease: the former including extension and number of component cells of the viable and the necrotic portions, the latter including the percentage of each cell variant that composes the active tumor fraction.

Our default simulation has been able to recapitulate the main aspects of primary tumor progression, such as host invasion, consumption of critical substrates and spatio-temporal evolution of phenotypic heterogeneity. In this regard, our virtual mass has been observed to differentiate in different regions: an internal necrotic core and an external rim of viable cells. In particular, more proliferative cell variants have been selected at the more internal areas of the active submasses whereas more aggressive clones have been detected at the tumor invasive edges.

Simulation setting	t_n [days]	t_F [days]	$d_a(t_F)/d_n(t_F)$	$N_a(t_F)/N_n(t_F)$	argmax(F)
reference simulation	14	22	2.9	2.8	1
inhibition of haptotaxis	20	41	2	1.8	1
increment in cell proliferative potential	9	22	1.9	1.8	0.8
increment in mutation events	14	22	2.9	2.8	1
tumor composed of only highly proliferating cells (i.e., with trait $y = 0$)	34	77	1.8	1.6	0
tumor composed of highly motile cells (i.e., with trait $y = 1$	14	21	3.1	3.9	1
absence of functional vasculature	0.1	no invasion	0	0	full necrosis
acute hypoxia	16	22	3	3	1
inhomogeneity of initial matrix profile	14	22	3.5	3.8	1

Table 2
Critical quantities characterizing tumor progression in the different scenarios previously taken into account.

We have then turned to analyze how tumor aggressiveness can be influenced by biophysical variations in the neoplastic cells themselves (intrinsic factors) or by manipulations of the microenvironment, that defines the ecology of those cells (extrinsic factors). We are going to discuss the resulting model outcomes in the forthcoming paragraphs.

Clinical and therapeutic implications. Surgical resection of tumors does not often result in a cure. A fraction of invasive cells may have already infiltrated the surrounding healthy and functional tissue therefore remaining after the removal of the main mass. This significantly contributes to the recurrence of the disease and poor prognosis.

Further, cancer cells with a predominant migratory phenotype are significantly unaffected by conventional cytotoxic treatments, which are frequently more efficient against proliferating cells. In fact, there is increasing evidence that invasive malignant cells with a low propensity to proliferate are significantly resistant to apoptosis (Giese et al. (2003)).

Any successful therapeutic strategy will indeed have (i) to treat the invasive portion of the tumor rather than the core lesion, i.e., it has to spatially contain the disease, and (ii) to limit the presence of highly motile cell variants in order to improve the efficacy of local treatments.

In this respect, we now review our results highlighting their potential in targeting more aggressive cell phenotypes as well as in restricting the invasive part of the tumor.

A decrement in cell motility due to inhibited haptotactic response implies reduced tumor expansion. In such a scenario (i) the malignant mass expands significantly slow, maintaining a compact morphology for a long period of time (i.e., tumor size after almost three weeks is nearly 30% smaller than its reference counterpart, cf. Figs. 5 (A) and 6 (C)) and (ii) necrosis involves a larger part of the disease (see Table 2). For all these considerations, disruption of haptotaxis can be therefore proposed as an interesting strategy to improve the success of an early tumor resection, despite such a biomedical intervention does not impact on the phenotypic heterogeneity of the mass, which remains characterized by the predominancy of highly proliferative cell clones (Table 2).

Targeting cell proliferation potential has instead contradictory effects. On one hand, enhanced duplication events within the mass result in a dramatic necrosis of the malignant tissue, in terms of both onset and extension of the metabolically dead portion of the malignancy (Table 2). On the other hand, a hyperproliferative disease is still characterized by the predominancy of highly aggressive cell phenotypes, that are able to reach the vasculature and therefore to initiate the metastatic cascade almost in the same time-lapse w.r.t. to the reference case (Table 2).

The proposed variation in cell mutation rate has instead little effect on tumor progression (Table 2). It is in fact an untargeted manipulation that does not substantially alter neither tumor size nor tumor composition. However, a legitimate clinical strategy may amount in increasing the possibility of mutations only in more motile cell variants. This intervention would in principle influence tumor phenotypic heterogeneity by selection of proliferating cell clones, whose predominance has significant implications. As demonstrated by our simulations and recapitulated in Table 2 a malignant mass mainly composed by highly proliferant individuals in fact poorly invades the tissue, thereby facilitating its removal.

Our model also shows that the progression of the virtual malignant mass is shaped by selective environmental pressures. In this respect, we predict that the absence of oxygen supply dramatically accelerates and enhances necrosis of our tumor which quickly undergoes metabolic death (Table 2). Our results are however in contrast with the paradigm developed by numerous clinical studies. For instance, hypoxic environmental conditions have been in fact shown to correlate with adverse prognosis and to render tumor cells more resistant to radiation and chemotherapy (Daruwalla and Christophi (2006); Kizaka-Kondoh et al. (2005); Hall et al. (2006)). Nutrient-poor hosts may also induce tumor fragmentation, recurrence and metastasis as well as drug resistance, as

computationally shown in Frieboes et al. (2009); Lowengrub et al. (2009); Sinek et al. (2009). In this respect, anti-angiogenic therapies may eventually give rise to the growth of aggressive multifocal tumors (De Jaeger et al. (2001); Lamszus et al. (2003); Rofstad and Halsør (2002)). This is probably due to the fact that we set a deterministic relationship between oxygen deprivation and necrosis. This aspect, as commented below, can of course be substantially improved. We also remark that a temporary inhibition of the activity of the physiological vasculature has little effect on tumor dynamics (Table 2).

Matrix spatial distribution around the damaged tissue is also important: in fact, specific ECM patterns may have no effect on tumor heterogeneity but may control the invasive behavior of the most aggressive cell variants, thereby reducing the invasive potential of the overall disease (Table 2). Selected migratory stimuli from the matrix may in fact counterbalance the selective pressure on cells to escape regions of scarce resources.

Taken together, our results suggest that relevant efficacy may derive from combined biomedical interventions. For instance, enhancement in the proliferative potential of a tumor could be efficiently coupled with a simultaneous disruption of cell motile behavior. The former can be obtained by increasing its oxygenation or affecting intracellular mitosis-related pathways, the latter by inhibition of integrins activity or by manipulation of the host structural matrix. The result could be a tumor characterized by a confined growth pattern and by the predominant presence of highly proliferative cell clones.

These considerations may be clinically relevant and contribute to therapeutic design but remain to be experimentally and clinically studied. However, they are in the same perspective of several results in cancer literature that predict the possible success of combined biomedical strategies. For instance, anti-invasive compounds (that increase intercellular adhesion and decrease cell mobility) may be successfully used as adjuvant to anti-angiogenic drugs (Bardelli et al. (1999); Bello et al. (2004); Date et al. (1998); Jain (2001)).

Model limitations and possible extensions. We conclude our work with a brief overview of possible model developments. First, the necessary relation between oxygen deprivation and necrosis can be substantially improved. In principle, normoxic cells change to an hypoxic state with a characteristic time dictated by the accumulation of the hypoxia-inducible factor 1alpha (HIF-1alpha), which starts when the intracellular chemical level drops under a certain limit. Hypoxic cells can recover their oxic phenotype if their internal amount of oxygen sufficiently increases again. Only a persistent lack of oxygen effectively induces necrotic transition. We may also reproduce in our modeling framework some phenotypic outcomes resulting from downstream cascades that activate in malignant cells as a response to hypoxia: they include secretion of proangiogenic factors, overproduction of matrix degrading enzymes, and decrement in intercellular adhesion (Erler et al. (2006); Kaur et al. (2005)). In addition, host tissues deprived of oxygen have been demonstrated to affect the metabolism of tumor cells, leading to activation of the glycolytic pathway, see for instance Gatenby et al. (2006) and references therein.

We have here also neglected the possibility for necrotic cells to induce the metabolic death of neighboring individuals by contact interactions (Oshiro et al. (2006)).

Our model has accounted for a phenotypic switch of viable cells only deriving from stochastic epigenetic mutations, i.e., implemented by the diffusive term in Eq. (2). However, a cancer cell (as any other tissue cell) can change its state also in response to varied internal or external signals. For instance, highly motile gliomas cells have been demonstrated to be able to revert to a proliferative program depending on the level of oxygenation (Giese et al. (2003); Keunen et al. (2011)). Such a model development would be particularly relevant from a therapeutic point of view. In fact, the phenotypic plasticity, i.e., the ability to switch among multiple phenotypes, represents an evolutionary advantage for cancer cells, used to evade therapy and metastasize (Brooks et al. (2015); Mooney et al. (2016); Roesch (2015); Varga et al. (2014)).

We have finally not included controlled cell suicide (apoptosis). This choice has been done since apoptosis neither correlates with prognosis nor has an impact on tumor volumetric extension and internal heterogeneity (Migheli et al. (1994); Schiffer et al. (1995)). Apoptosis is in fact a process that is active for all cell variants. It could be however incorporated into our model by simply varying the effective cell proliferation rates in Eq. (2).

In principle our model can be applied to reproduce the main aspects of the avascular growth of any type of tumor. This would of course require a more specific parametrization and the use of domain configurations able to better describe the tissue of interest but, at the same time, it would allow to have a detailed quantitative validation of the resulting computational outcomes.

Acknowledgements

This research was partially supported by the Italian Ministry of Education, University and Research (MIUR) through the "Dipartimenti di Eccellenza" Programme (2018-2022) – Dipartimento di Scienze Matematiche "G. L. Lagrange", Politecnico di Torino (CUP: E11G18000350001). All authors are members of GNFM (Gruppo Nazionale per la Fisica Matematica) of INdAM (Istituto Nazionale di Alta Matematica).

Conflict of interest

The authors declare that they have no conflict of interest.

References

Abramovitch, R., Meir, G., Neeman, M., 1995. Neovascularization induced growth of implanted C6 glioma multicellular spheroids: magnetic resonance microimaging. Cancer Research 55, 1956–1962.

Adam, J.A., 1997. General aspects of modeling tumor growth and immune response, in: A survey of models for tumor-immune system dynamics. Springer, pp. 15–87.

Alberts, B., Johnson, A.D., Lewis, J., Raff, M., Roberts, K., Walter, P., 2002. Molecular biology of the cell, 4th edn. Garland Science, New York .

Anderson, A.R., Chaplain, M.A., 1998. Continuous and discrete mathematical models of tumor-induced angiogenesis. Bulletin of Mathematical Biology 60, 857–899.

Anderson, A.R., Chaplain, M.A., Newman, E.L., Steele, R.J., Thompson, A.M., 2000. Mathematical modelling of tumour invasion and metastasis. Computational and Mathematical Methods in Medicine 2, 129–154.

Anderson, A.R., Quaranta, V., 2008. Integrative mathematical oncology. Nature Reviews Cancer 8, 227–234.

Araujo, R.P., McElwain, D.L., 2004. A history of the study of solid tumour growth: the contribution of mathematical modelling. Bulletin of Mathematical Biology 66, 1039–1091.

Ardaševa, A., Gatenby, R.A., Anderson, A.R., Byrne, H.M., Maini, P.K., Lorenzi, T., 2020. A mathematical dissection of the adaptation of cell populations to fluctuating oxygen levels. Bulletin of Mathematical Biology 82, 1–24.

Bardelli, A., Basile, M.L., Audero, E., Giordano, S., Wennström, S., Ménard, S., Comoglio, P.M., Ponzetto, C., 1999. Concomitant activation of pathways downstream of Grb2 and PI 3-kinase is required for MET-mediated metastasis. Oncogene 18, 1139–1146.

Bayer, C., Vaupel, P., 2012. Acute versus chronic hypoxia in tumors. Strahlentherapie und Onkologie 188, 616–627.

Bello, L., Lucini, V., Costa, F., Pluderi, M., Giussani, C., Acerbi, F., Carrabba, G., Pannacci, M., Caronzolo, D., Grosso, S., Shinkaruk, S., Colleoni, F., Canron, X., Tomei, G., Deleris, G., Bikfalvi, A., 2004. Combinatorial administration of molecules that simultaneously inhibit angiogenesis and invasion leads to increased therapeutic efficacy in mouse models of malignant glioma. Clinical Cancer Research 10, 4527–4537.

Bellomo, N., Li, N.K., Maini, P.K., 2008. On the foundations of cancer modelling: selected topics, speculations, and perspectives. Mathematical Models and Methods in Applied Sciences 18, 593–646.

Bellomo, N., Preziosi, L., 2000. Modelling and mathematical problems related to tumor evolution and its interaction with the immune system. Mathematical and Computer Modelling 32, 413–452.

Benzekry, S., Lamont, C., Beheshti, A., Tracz, A., Ebos, J.M., Hlatky, L., Hahnfeldt, P., 2014. Classical mathematical models for description and prediction of experimental tumor growth. PLoS Computational Biology 10, e1003800.

Brooks, M.D., Burness, M.L., Wicha, M.S., 2015. Therapeutic implications of cellular heterogeneity and plasticity in breast cancer. Cell Stem Cell 17, 260–271.

Brown, J.M., Wilson, W.R., 2004. Exploiting tumour hypoxia in cancer treatment. Nature Reviews Cancer 4, 437–447.

Burleson, K.M., Boente, M.P., Pambuccian, S.E., Skubitz, A.P., 2006. Disaggregation and invasion of ovarian carcinoma ascites spheroids. Journal of Translational Medicine 4, 1–16.

Byrne, H.M., Alarcon, T., Owen, M.R., Webb, S.D., Maini, P.K., 2006. Modelling aspects of cancer dynamics: a review. Philosophical Transactions of the Royal Society A: Mathematical, Physical and Engineering Sciences 364, 1563–1578.

Carey, S.P., Starchenko, A., McGregor, A.L., Reinhart-King, C.A., 2013. Leading malignant cells initiate collective epithelial cell invasion in a three-dimensional heterotypic tumor spheroid model. Clinical & experimental metastasis 30, 615–630.

Castro, M.A., Klamt, F., Grieneisen, V.A., Grivicich, I., Moreira, J.C., 2003. Gompertzian growth pattern correlated with phenotypic organization of colon carcinoma, malignant glioma and non-small cell lung carcinoma cell lines. Cell Proliferation 36, 65–73.

Cattaneo, C., 1952. A form of heat conduction equation which eliminates the paradox of instantaneous propagation. Compte Rendus 247, 431–433.

Chaplain, M.A., 1996. Avascular growth, angiogenesis and vascular growth in solid tumours: The mathematical modelling of the stages of tumour development. Mathematical and Computer Modelling 23, 47–87.

Cristini, V., Lowengrub, J., 2010. Multiscale modeling of cancer: An integrated experimental and mathematical modeling approach. Cambridge University Press.

Cumsille, P., Coronel, A., Conca, C., Quiñinao, C., Escudero, C., 2015. Proposal of a hybrid approach for tumor progression and tumor-induced angiogenesis. Theoretical Biology and Medical Modelling 12, 13.

Daruwalla, J., Christophi, C., 2006. Hyperbaric oxygen therapy for malignancy: a review. World Journal of Surgery 30, 2112–2131.

Daşu, A., Toma-Daşu, I., Karlsson, M., 2003. Theoretical simulation of tumour oxygenation and results from acute and chronic hypoxia. Physics in Medicine & Biology 48, 2829.

Date, K., Matsumoto, K., Kuba, K., Shimura, H., Tanaka, M., Nakamura, T., 1998. Inhibition of tumor growth and invasion by a four-kringle antagonist (HGF/NK4) for hepatocyte growth factor. Oncogene 17, 3045–3054.

De Jaeger, K., Kavanagh, M.C., Hill, R.P., 2001. Relationship of hypoxia to metastatic ability in rodent tumours. British Journal of Cancer 84, 1280–1285.

Diao, W., Tong, X., Yang, C., Zhang, F., Bao, C., Chen, H., Liu, L., Li, M., Ye, F., Fan, Q., Wang, J., Ou-Yang, Z.C., 2019. Behaviors of glioblastoma cells in in vitro microenvironments. Scientific Reports 9, 1–9.

Doerfler, W., Böhm, P., 2006. DNA methylation: development, genetic disease and cancer. volume 310. Springer Science & Business Media.

Duesberg, P., Stindl, R., Hehlmann, R., 2000. Explaining the high mutation rates of cancer cells to drug and multidrug resistance by chromosome reassortments that are catalyzed by aneuploidy. Proceedings of the National Academy of Sciences 97, 14295–14300.

Eftimie, R., Bramson, J.L., Earn, D.J., 2011. Interactions between the immune system and cancer: a brief review of non-spatial mathematical models. Bulletin of Mathematical Biology 73, 2–32.

Enam, S.A., Klaus, E., 1998. Role of extracellular matrix in tumor invasion: migration of glioma cells along fibronectin-positive mesenchymal cell processes. Neurosurgery 42, 599–608.

Engler, A., Bacakova, L., Newman, C., Hategan, A., Griffin, M., Discher, D., 2004. Substrate compliance versus ligand density in cell on gel responses. Biophysical Journal 86, 617–628.

Erler, J.T., Bennewith, K.L., Nicolau, M., Dornhöfer, N., Kong, C., Le, Q.T., Chi, J.T.A., Jeffrey, S.S., Giaccia, A.J., 2006. Lysyl oxidase is essential for hypoxia-induced metastasis. Nature 440, 1222–1226.

Fiandaca, G., Delitala, M., Lorenzi, T., 2021. A mathematical study of the influence of hypoxia and acidity on the evolutionary dynamics of cancer. Bull. Math. Biol. 83.

Folkman, J., Hochberg, M., 1973. Self-regulation of growth in three dimensions. The Journal of Experimental Medicine 138, 745–753.

Freyer, J.P., Sutherland, R.M., 1983. Determination of diffusion constants for metabolites in multicell tumor spheroids, in: Oxygen Transport to Tissue—IV. Springer, pp. 463–475.

Freyer, J.P., Sutherland, R.M., 1986. Regulation of growth saturation and development of necrosis in EMT6/Ro multicellular spheroids by the glucose and oxygen supply. Cancer Research 46, 3504–3512.

Frieboes, H.B., Edgerton, M.E., Fruehauf, J.P., Rose, F.R., Worrall, L.K., Gatenby, R.A., Ferrari, M., Cristini, V., 2009. Prediction of drug response in breast cancer using integrative experimental/computational modeling. Cancer Research 69, 4484–4492.

Friedl, P., Wolf, K., 2003. Tumour-cell invasion and migration: diversity and escape mechanisms. Nature Reviews Cancer 3, 362–374.

Friedman, A., 2004. A hierarchy of cancer models and their mathematical challenges. Discrete & Continuous Dynamical Systems-B 4, 147.

Friedman, A., 2007. Mathematical analysis and challenges arising from models of tumor growth. Mathematical Models and Methods in Applied Sciences 17, 1751–1772.

Gaggioli, C., Hooper, S., Hidalgo-Carcedo, C., Grosse, R., Marshall, J.F., Harrington, K., Sahai, E., 2007. Fibroblast-led collective invasion of carcinoma cells with differing roles for RhoGTPases in leading and following cells. Nature Cell Biology 9, 1392–1400.

Gallaher, J.A., Brown, J.S., Anderson, A.R., 2019. The impact of proliferation-migration tradeoffs on phenotypic evolution in cancer. Scientific Reports 9, 1–10.

Gao, C.F., Xie, Q., Su, Y.L., Koeman, J., Khoo, S.K., Gustafson, M., Knudsen, B.S., Hay, R., Shinomiya, N., Vande Woude, G.F., 2005. Proliferation and invasion: plasticity in tumor cells. Proceedings of the National Academy of Sciences 102, 10528–10533.

Gatenby, R.A., Gawlinski, E.T., Gmitro, A.F., Kaylor, B., Gillies, R.J., 2006. Acid-mediated tumor invasion: a multidisciplinary study. Cancer Research 66, 5216–5223.

Gatenby, R.A., Smallbone, K., Maini, P.K., Rose, F., Averill, J., Nagle, R.B., Worrall, L., Gillies, R.J., 2007. Cellular adaptations to hypoxia and acidosis during somatic evolution of breast cancer. British Journal of Cancer 97, 646–653.

Gaudet, C., Marganski, W.A., Kim, S., Brown, C.T., Gunderia, V., Dembo, M., Wong, J.Y., 2003. Influence of type I collagen surface density on fibroblast spreading, motility, and contractility. Biophysical Journal 85, 3329–3335.

Giese, A., Bjerkvig, R., Berens, M.E., Westphal, M., 2003. Cost of migration: invasion of malignant gliomas and implications for treatment. Journal of Clinical Oncology 21, 1624–1636.

Giese, A., Kluwe, L., Laube, B., Meissner, H., Berens, M.E., Westphal, M., 1996a. Migration of human glioma cells on myelin. Neurosurgery 38, 755–764.

Giese, A., Loo, M.A., Tran, N., Haskett, D., Coons, S.W., Berens, M.E., 1996b. Dichotomy of astrocytoma migration and proliferation. International Journal of Cancer 67, 275–282.

Grimes, D.R., Kelly, C., Bloch, K., Partridge, M., 2014. A method for estimating the oxygen consumption rate in multicellular tumour spheroids. Journal of The Royal Society Interface 11, 20131124.

Hall, E.J., Giaccia, A.J., et al., 2006. Radiobiology for the Radiologist. volume 6. Philadelphia.

Hanahan, D., Weinberg, R.A., 2011. Hallmarks of cancer: the next generation. Cell 144, 646–674.

Harris, A.L., 2002. Hypoxia—a key regulatory factor in tumour growth. Nature Reviews Cancer 2, 38–47.

Hatzikirou, H., Basanta, D., Simon, M., Schaller, K., Deutsch, A., 2012. 'Go or grow': the key to the emergence of invasion in tumour progression? Mathematical Medicine and Biology: A Journal of the IMA 29, 49–65.

Hausser, J., Alon, U., 2020. Tumour heterogeneity and the evolutionary trade-offs of cancer. Nature Reviews Cancer 20, 247–257.

Höckel, M., Schlenger, K., Aral, B., Mitze, M., Schäffer, U., Vaupel, P., 1996. Association between tumor hypoxia and malignant progression in advanced cancer of the uterine cervix. Cancer Research 56, 4509–4515.

Ilina, O., Bakker, G.J., Vasaturo, A., Hoffman, R.M., Friedl, P., 2011. Two-photon laser-generated microtracks in 3D collagen lattices: principles of MMP-dependent and-independent collective cancer cell invasion. Physical Biology 8, 015010.

Irimia, D., Toner, M., 2009. Spontaneous migration of cancer cells under conditions of mechanical confinement. Integrative Biology 1, 506–512.

Jain, R.K., 2001. Normalizing tumor vasculature with anti-angiogenic therapy: a new paradigm for combination therapy. Nature Medicine 7, 987–989.

Kaur, B., Khwaja, F.W., Severson, E.A., Matheny, S.L., Brat, D.J., Van Meir, E.G., 2005. Hypoxia and the hypoxia-inducible-factor pathway in glioma growth and angiogenesis. Neuro-Oncology 7, 134–153.

Kenny, H.A., Kaur, S., Coussens, L.M., Lengyel, E., 2008. The initial steps of ovarian cancer cell metastasis are mediated by MMP-2 cleavage of vitronectin and fibronectin. The Journal of Clinical Investigation 118, 1367–1379.

Keunen, O., Johansson, M., Oudin, A., Sanzey, M., Rahim, S.A.A., Fack, F., Thorsen, F., Taxt, T., Bartos, M., Jirik, R., Miletic, H., Wang, J., Stieber, D., Stuhr, L., Moen, I., Rygh, C.B., Bjerkvig, R., Niclou, S.P., 2011. Anti-VEGF treatment reduces blood supply and increases tumor cell invasion in glioblastoma. Proceedings of the National Academy of Sciences 108, 3749–3754.

Khaitan, D., Chandna, S., Arya, M.B., Dwarakanath, B.S., 2006. Establishment and characterization of multicellular spheroids from a human glioma cell line; Implications for tumor therapy. Journal of Translational Medicine 4, 1–13.

Kizaka-Kondoh, S., Inoue, M., Harada, H., Hiraoka, M., 2005. Tumor hypoxia: a target for selective cancer therapy. Cancer Science 94, 1021–1028.

Lamszus, K., Kunkel, P., Westphal, M., 2003. Invasion as limitation to anti-angiogenic glioma therapy. Local Therapies for Glioma Present Status and Future Developments , 169–177.

Lefranc, F., Brotchi, J., Kiss, R., 2005. Possible future issues in the treatment of glioblastomas: special emphasis on cell migration and the resistance of migrating glioblastoma cells to apoptosis. Journal of Clinical Oncology 23, 2411–2422.

LeVeque, R.J., 2007. Finite difference methods for ordinary and partial differential equations: steady-state and time-dependent problems. SIAM.

Liu, S., Cong, Y., Wang, D., Sun, Y., Deng, L., Liu, Y., Martin-Trevino, R., Shang, L., McDermott, S.P., Landis, M.D., et al., 2014. Breast cancer stem cells transition between epithelial and mesenchymal states reflective of their normal counterparts. Stem Cell Reports 2, 78–91.

Lorenzi, T., Lorz, A., Perthame, B., 2017. On interfaces between cell populations with different mobilities. Kinetic and Related Models 10, 299–311.

Lorenzi, T., Perthame, B., Ruan, X., 2020. Invasion fronts and adaptive dynamics in a model for the growth of cell populations with heterogeneous mobility. arXiv preprint arXiv:2007.13084 .

Lorenzi, T., Perthame, B., Ruan, X., 2021. Invasion fronts and adaptive dynamics in a model for the growth of cell populations with heterogeneous mobility. Eur. J. Appl. Math. , 1–18.

Lorenzi, T., Venkataraman, C., Lorz, A., Chaplain, M.A., 2018. The role of spatial variations of abiotic factors in mediating intratumour phenotypic heterogeneity. Journal of Theoretical Biology 451, 101–110.

Lowengrub, J.S., Frieboes, H.B., Jin, F., Chuang, Y.L., Li, X., Macklin, P., Wise, S.M., Cristini, V., 2009. Nonlinear modelling of cancer: bridging the gap between cells and tumours. Nonlinearity 23, R1.

Maley, C.C., Aktipis, A., Graham, T.A., Sottoriva, A., Boddy, A.M., Janiszewska, M., Silva, A.S., Gerlinger, M., Yuan, Y., Pienta, K.J., Anderson, K.S., Gatenby, R., Swanton, C., Posada, D., Chung-I, W., Schiffman, J.D., Hwang, E.S., Polyak, K., Anderson, A.R., Brown, J.S., Greaves, M., Shibata, D., 2017. Classifying the evolutionary and ecological features of neoplasms. Nature Reviews Cancer 17, 605–619.

Martínez-González, A., Calvo, G.F., Pérez Romasanta, L.A., Pérez-García, V.M., 2012. Hypoxic cell waves around necrotic cores in glioblastoma: a biomathematical model and its therapeutic implications. Bulletin of Mathematical Biology 74, 2875–2896.

McFarland, C.D., Korolev, K.S., Kryukov, G.V., Sunyaev, S.R., Mirny, L.A., 2013. Impact of deleterious passenger mutations on cancer progression. Proceedings of the National Academy of Sciences 110, 2910–2915.

McFarland, C.D., Mirny, L.A., Korolev, K.S., 2014. Tug-of-war between driver and passenger mutations in cancer and other adaptive processes. Proceedings of the National Academy of Sciences 111, 15138–15143.

Mehlen, P., Puisieux, A., 2006. Metastasis: a question of life or death. Nature reviews cancer 6, 449–458.

Migheli, A., Cavalla, P., Marino, S., Schiffer, D., 1994. A study of apoptosis in normal and pathologic nervous tissue after in situ end-labeling of DNA strand breaks. Journal of Neuropathology & Experimental Neurology 53, 606–616.

Mooney, S.M., Jolly, M.K., Levine, H., Kulkarni, P., 2016. Phenotypic plasticity in prostate cancer: role of intrinsically disordered proteins. Asian Journal of Andrology 18, 704.

Moore, N., Houghton, J., Lyle, S., 2012. Slow-cycling therapy-resistant cancer cells. Stem Cells and Development 21, 1822–1830.

Moreira, J., Deutsch, A., 2002. Cellular automaton models of tumor development: a critical review. Advances in Complex Systems 5, 247–267.

Mueller-Klieser, W.F., Sutherland, R.M., 1984. Oxygen consumption and oxygen diffusion properties of multicellular spheroids from two different cell lines, in: Oxygen Transport to Tissue—VI. Springer, pp. 311–321.

Murphy, G., Gavrilovic, J., 1999. Proteolysis and cell migration: creating a path?. Current Opinion in Cell Biology 11, 614–621.

Oraiopoulou, M.E., Tzamali, E., Tzedakis, G., Vakis, A., Papamatheakis, J., Sakkalis, V., 2017. *In vitro/in silico* study on the role of doubling time heterogeneity among primary glioblastoma cell lines. BioMed research international 2017.

Osada, H., Takahashi, T., 2002. Genetic alterations of multiple tumor suppressors and oncogenes in the carcinogenesis and progression of lung cancer. Oncogene 21, 7421–7434.

Oshiro, S., Tsugu, H., Komatsu, F., Ohnishi, H., Ueno, Y., Sakamoto, S., Fukushima, T., Soma, G.I., 2006. Evaluation of intratumoral administration of tumor necrosis factor-alpha in patients with malignant glioma. Anticancer research 26, 4027–4032.

Parker, J.J., Canoll, P., Niswander, L., Kleinschmidt-DeMasters, B.K., Foshay, K., Waziri, A., 2018. Intratumoral heterogeneity of endogenous tumor cell invasive behavior in human glioblastoma. Scientific Reports 8, 1–10.

Perthame, B., 2006. Transport equations in biology. Springer Science & Business Media.

Perthame, B., Quirós, F., Vázquez, J.L., 2014. The Hele–Shaw asymptotics for mechanical models of tumor growth. Archive for Rational Mechanics and Analysis 212, 93–127.

Pogue, B.W., O'Hara, J.A., Wilmot, C.M., Paulsen, K.D., Swartz, H.M., 2001. Estimation of oxygen distribution in RIF-1 tumors by diffusion model-based interpretation of pimonidazole hypoxia and Eppendorf measurements. Radiation Research 155, 15–25.

Preziosi, L., 2003. Cancer modelling and simulation. CRC Press.

Quaranta, V., Weaver, A.M., Cummings, P.T., Anderson, A.R., 2005. Mathematical modeling of cancer: the future of prognosis and treatment. Clinica Chimica Acta 357, 173–179.

Risom, T., Langer, E.M., Chapman, M.P., Rantala, J., Fields, A.J., Boniface, C., Alvarez, M.J., Kendsersky, N.D., Pelz, C.R., Johnson-Camacho, K., Dobrolecki, L.E., Chin, K., Aswani, A.J., Wang, N.J., Califano, A., Lewis, M.T., Tomlin, C.J., Spellman, P.T., Adey, A., Gray, J.W., Sears, R.C., 2018. Differentiation-state plasticity is a targetable resistance mechanism in basal-like breast cancer. Nature Communications 9, 1–17.

Roesch, A., 2015. Tumor heterogeneity and plasticity as elusive drivers for resistance to MAPK pathway inhibition in melanoma. Oncogene 34, 2951–2957.

Rofstad, E.K., Halsør, E., 2002. Hypoxia-associated spontaneous pulmonary metastasis in human melanoma xenografts: involvement of microvascular hot spots induced in hypoxic foci by interleukin 8. British Journal of Cancer 86, 301–308.

Salsa, S., 2016. Partial differential equations in action: from modelling to theory. volume 99. Springer.

Schiffer, D., Cavalla, P., Migheli, A., Chiò, A., Giordana, M.T., Marino, S., Attanasio, A., 1995. Apoptosis and cell proliferation in human neuroepithelial tumors. Neuroscience Letters 195, 81–84.

Scianna, M., Preziosi, L., 2012a. Hybrid cellular potts model for solid tumor growth, in: New Challenges for Cancer Systems Biomedicine. Springer, pp. 205–224.

Scianna, M., Preziosi, L., 2012b. A hybrid model describing different morphologies of tumor invasion fronts. Mathematical Modelling of Natural Phenomena 7, 78–104.

Shashni, B., Ariyasu, S., Takeda, R., Suzuki, T., Shiina, S., Akimoto, K., Maeda, T., Aikawa, N., Abe, R., Osaki, T., Itoh, N., Aoki, S., 2018. Size-based differentiation of cancer and normal cells by a particle size analyzer assisted by a cell-recognition PC software. Biological and Pharmaceutical Bulletin 41, 487–503.

Shield, K., Ackland, M.L., Ahmed, N., Rice, G.E., 2009. Multicellular spheroids in ovarian cancer metastases: Biology and pathology. Gynecologic Oncology 113, 143–148.

Sinek, J.P., Sanga, S., Zheng, X., Frieboes, H.B., Ferrari, M., Cristini, V., 2009. Predicting drug pharmacokinetics and effect in vascularized tumors using computer simulation. Journal of Mathematical Biology 58, 485–510.

Spratt, J.S., Meyer, J.S., Spratt, J.A., 1995. Rates of growth of human solid neoplasms: Part I. Journal of Surgical Oncology 60, 137–146.

Staneva, R., El Marjou, F., Barbazan, J., Krndija, D., Richon, S., Clark, A.G., Vignjevic, D.M., 2019. Cancer cells in the tumor core exhibit spatially coordinated migration patterns. Journal of Cell Science 132.

Stearns, S.C., 1989. Trade-offs in life-history evolution. Functional Ecology 3, 259–268.

Stein, A.M., Demuth, T., Mobley, D., Berens, M., Sander, L.M., 2007. A mathematical model of glioblastoma tumor spheroid invasion in a three-dimensional in vitro experiment. Biophysical Journal 92, 356–365.

Swanson, K.R., Rockne, R.C., Claridge, J., Chaplain, M.A., Alvord, E.C., Anderson, A.R., 2011. Quantifying the role of angiogenesis in malignant progression of gliomas: in silico modeling integrates imaging and histology. Cancer Research 71, 7366–7375.

Tannock, I.F., 1972. Oxygen diffusion and the distribution of cellular radiosensitivity in tumours. The British Journal of Radiology 45, 515–524.

Trucu, D., Domschke, P., Gerisch, A., Chaplain, M.A., 2016. Multiscale computational modelling and analysis of cancer invasion, in: Mathematical Models and Methods for Living Systems. Springer, pp. 275–321.

Varga, J., De Oliveira, T., Greten, F.R., 2014. The architect who never sleeps: tumor-induced plasticity. FEBS Letters 588, 2422–2427.

Vazquez, J., 2012. Barenblatt solutions and asymptotic behaviour for a nonlinear fractional heat equation of porous medium type. Journal of the European Mathematical Society 16.

Villa, C., Chaplain, M.A., Lorenzi, T., 2021. Modeling the emergence of phenotypic heterogeneity in vascularized tumors. SIAM Journal on Applied Mathematics 81, 434–453.

Ward, J.P., King, J.R., 1997. Mathematical modelling of avascular-tumour growth. Mathematical Medicine and Biology: A Journal of the IMA 14, 39–69.

Wolf, K., Mazo, I., Leung, H., Engelke, K., Von Andrian, U.H., Deryugina, E.I., Strongin, A.Y., BroHERE!HERE!cker, E.B., Friedl, P., 2003. Compensation mechanism in tumor cell migration: mesenchymal–amoeboid transition after blocking of pericellular proteolysis. The Journal of Cell Biology 160, 267–277.

Zhigun, A., Surulescu, C., Hunt, A., 2018. A strongly degenerate diffusion-haptotaxis model of tumour invasion under the go-or-grow dichotomy hypothesis. Mathematical Methods in the Applied Sciences 41, 2403–2428.

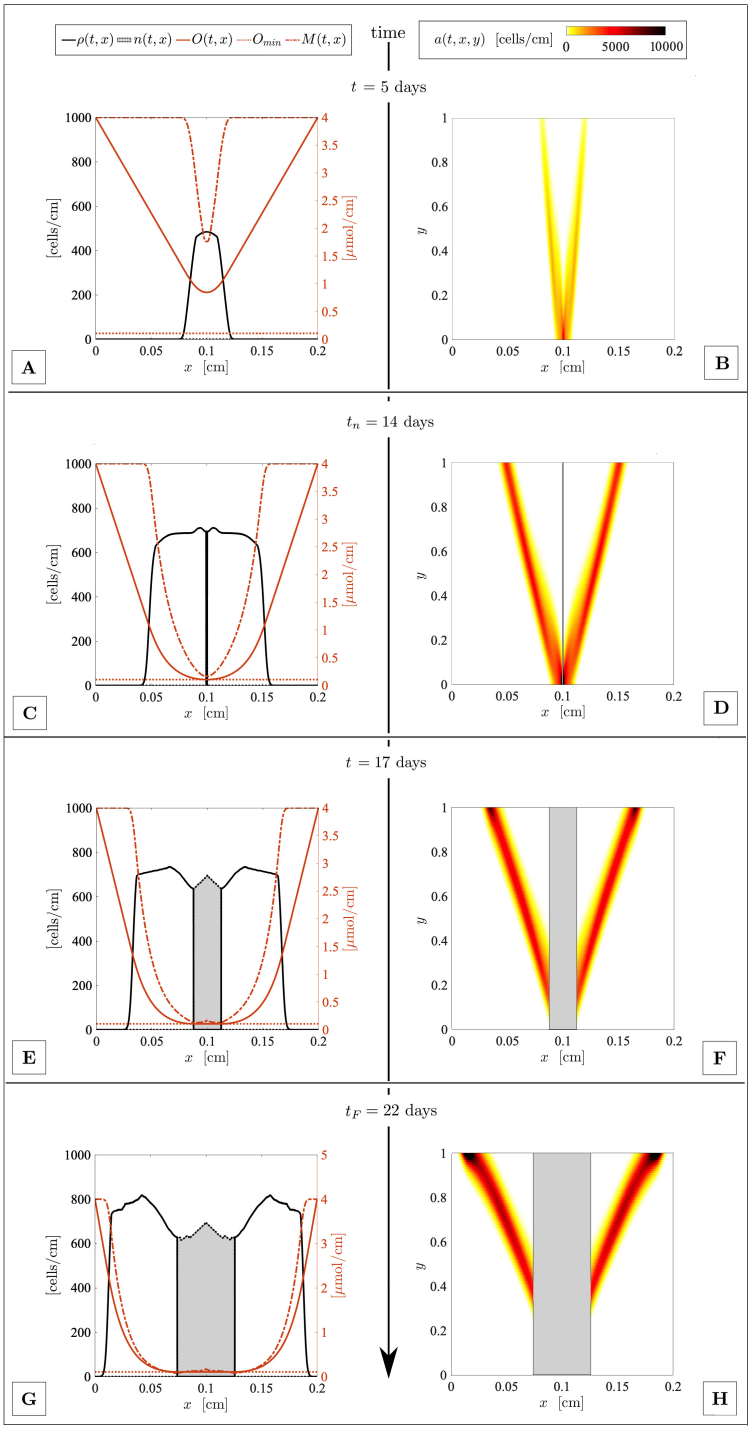

Figure 4: Reference simulation. The tumor starts to radially expand within the tissue as a consequence of the invasive capacity of motile cell clones. The oxygen level at the center of the malignant mass then drops to the basal level O_{min}, therefore causing localized necrotic transition. In the subsequent phases, we observe the enlargement of the necrotic core and the simultaneous invasion of the host due to the expansion of the peripheral regions of the tumor, populated by the highly aggressive cells. At the end of the simulation, fronts of fully motile individuals are able to reach the vasculature present at both domain edges. The gray-shadowed rectangles within the graphs in the right column show the position of the necrotic core of the tumor.

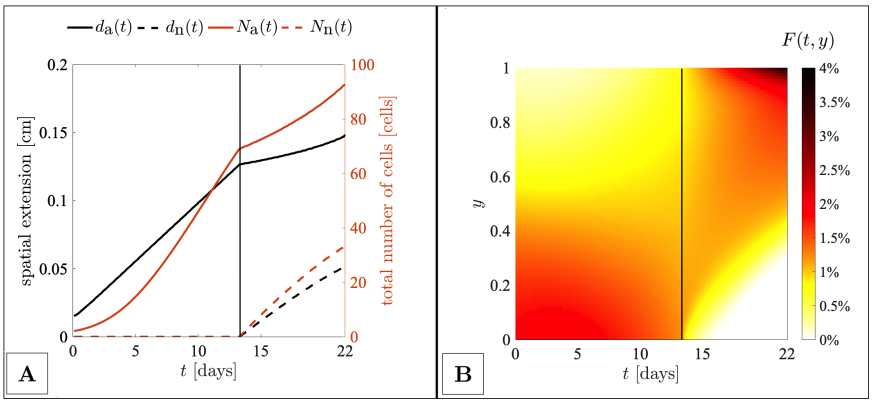

Figure 5: (A) Time evolution of tumor morphological determinants, i.e., extension of the tumor necrotic core, of the viable region and of the corresponding cell number. (B) Time evolution of the phenotypic heterogeneity characterizing the tumor mass. As defined in Eq. (18), F evaluates in fact the global fraction of each variant of viable cells. In both panels, the black vertical line indicates t_n.

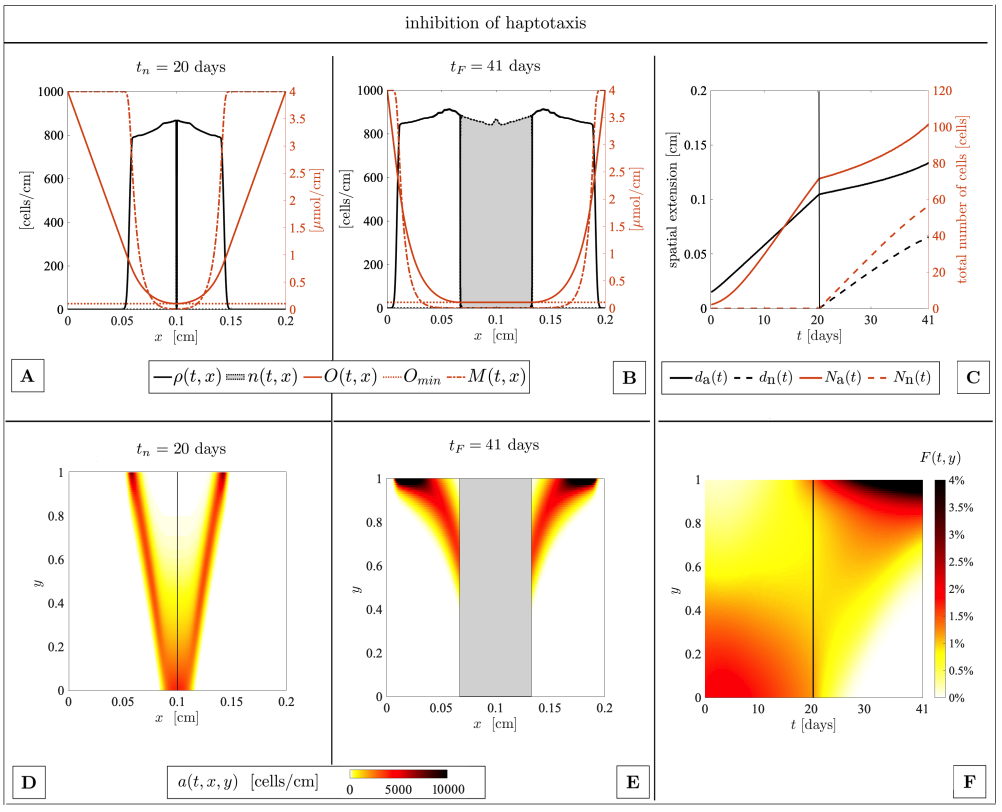

Figure 6: Tumor growth in the case of inhibition of the haptotactic mechanism, i.e., obtained by setting $w_2 = 0$ in Eq. (2). Before the onset of necrosis, the malignant mass is characterized by decreased invasive potential but enhanced cell density. Such a lower aggressiveness of the disease is maintained also in the late stages of growth (i.e., after t_n). The necrotic part of the tumor in fact enlarges more rapidly than the rest of the mass the and the tissue is completely compromised nearly three weeks later than in the reference case. Along the entire observation period, the tumor is characterized by high heterogeneity, i.e., by the local coexistence of a wide range of cell variants. Finally, a large spectrum of cell phenotypes undergoes necrotic transition since the reduced migratory capacity decreases the possibility to escape hypoxia. In panels (C) and (F), the black vertical line indicates t_n.

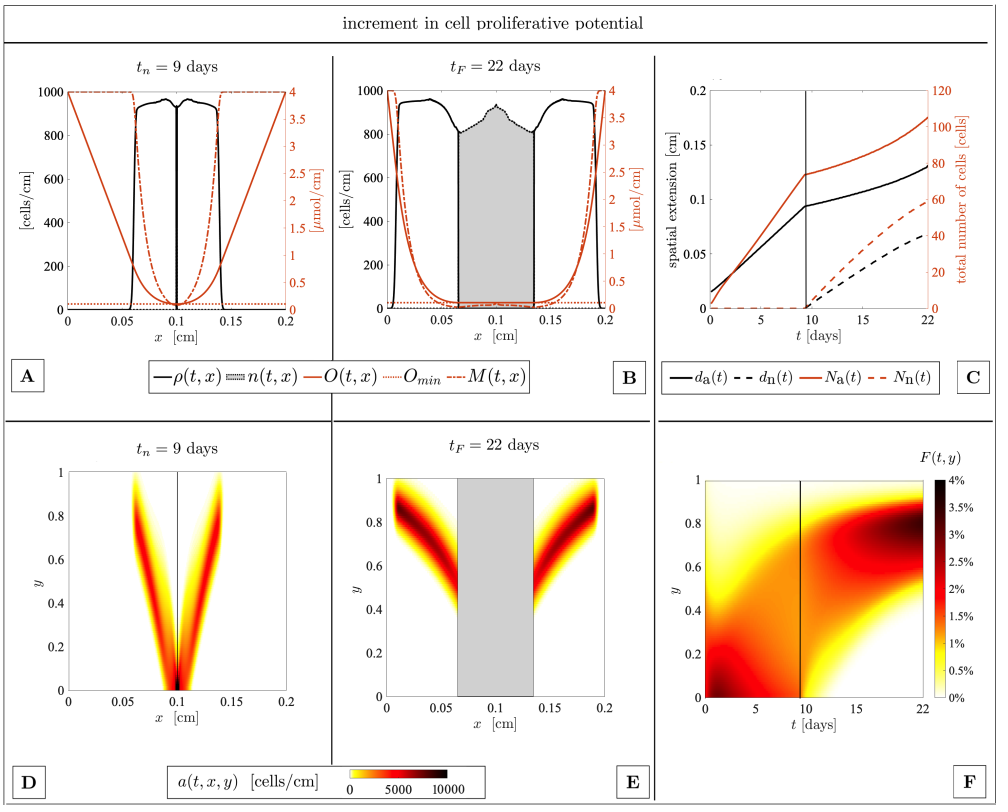

Figure 7: Tumor growth in the case of increment in cell proliferation potential, i.e., obtained by increasing of one order of magnitude the value of $\gamma_{\max}$ in Eq. (7). In the early stages of development, the malignancy is an overdense mass that poorly invades the host tissue. Necrosis quickly occurs, due to the rapid drop of oxygen at the center of the tissue. In the late phases of progression (i.e., after t_n) the necrotic fraction rapidly enlarges and occupies most part of the mass, whereas the tissue is completely compromised at 22 days, i.e., at the same time as in the reference case. Along the entire observation period, the tumor is characterized by high heterogeneity, i.e., by the local coexistence of a wide range of cell variants. Finally, a wide spectrum of cell phenotypes undergoes necrosis due to the dramatic consumption of available oxygen. In panels (C) and (F), the black vertical line indicates t_n.

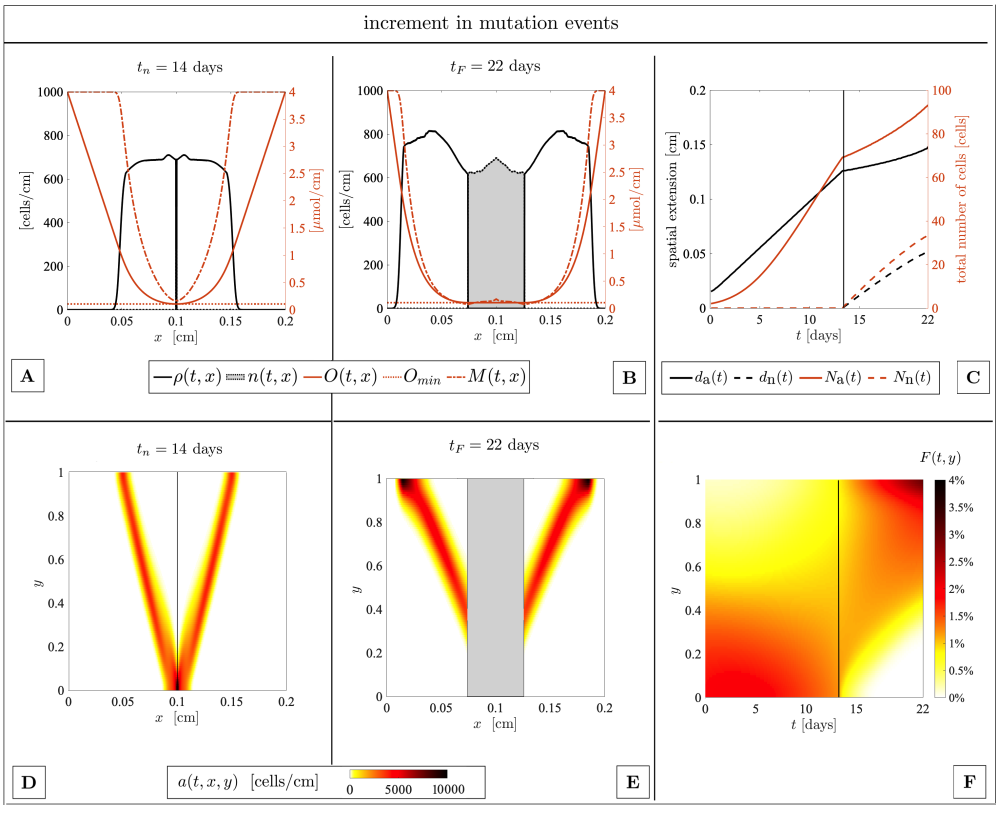

Figure 8: Tumor growth in the case of enhanced mutation rate across the mass, i.e., obtained by increasing the value of D_a in Eq. (2). The macroscopic evolution of the disease does not vary upon such a model manipulation. In fact, the spatio-temporal evolution of the viable and the necrotic portions of the malignancy is close to the counterpart observed in the reference case. On the opposite, differences arise at the microscopic level. In fact, tumor heterogeneity is higher, as all cell variants are present in larger volume fractions of the mass. As in the reference simulation, also in this case, the necrotic transition causes the disappearance of active cells whose trait is lower than 0.3. In panels (C) and (F), the black vertical line indicates t_n.

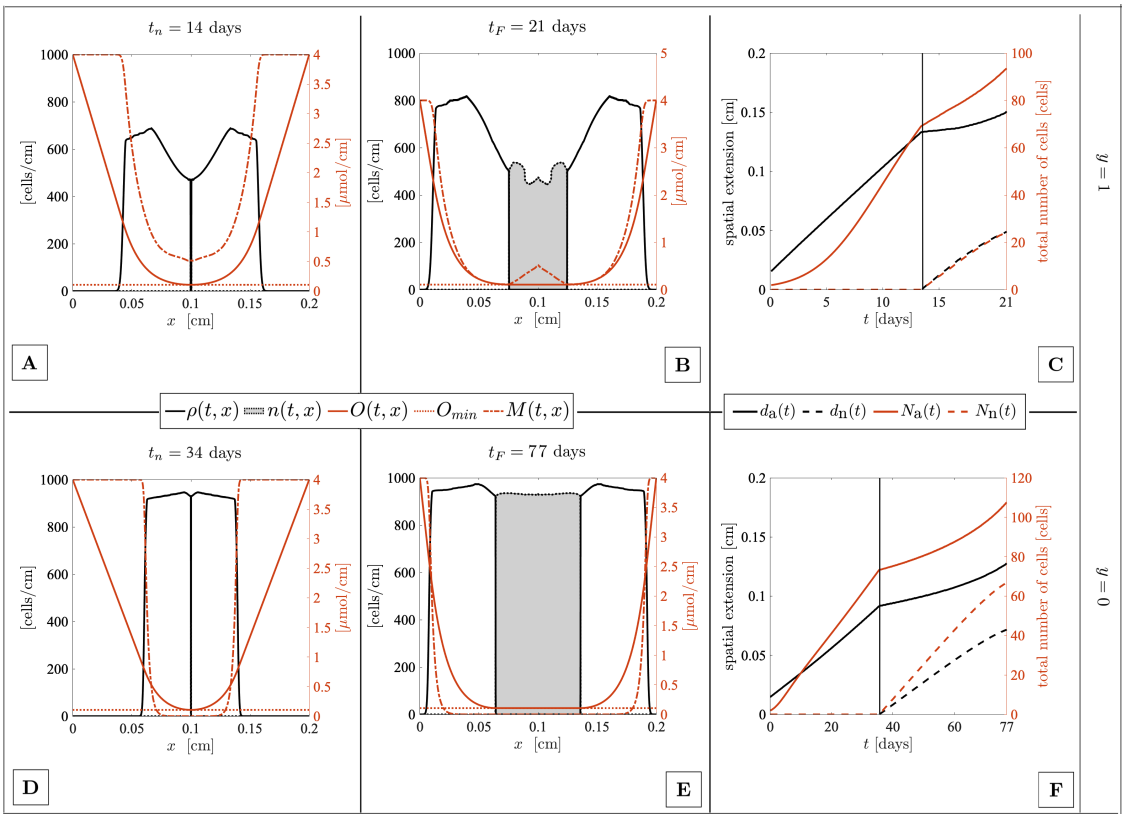

Figure 9: Growth of homogeneous masses, i.e., formed either by cells with the maximal migratory capacity (with trait $y = 1$, top panels) or by cells with the maximal proliferation potential (with trait $y = 0$, bottom panels). A tumor composed of highly motile cells is characterized by a poor necrosis, which is instead significant in the case of a tumor composed of highly proliferating individuals. In such a second scenario, the invasion of the tissue is very slow, as it is completed nearly 2 months later than in the reference case. In panels (C) and (F), the black vertical line indicates t_n.

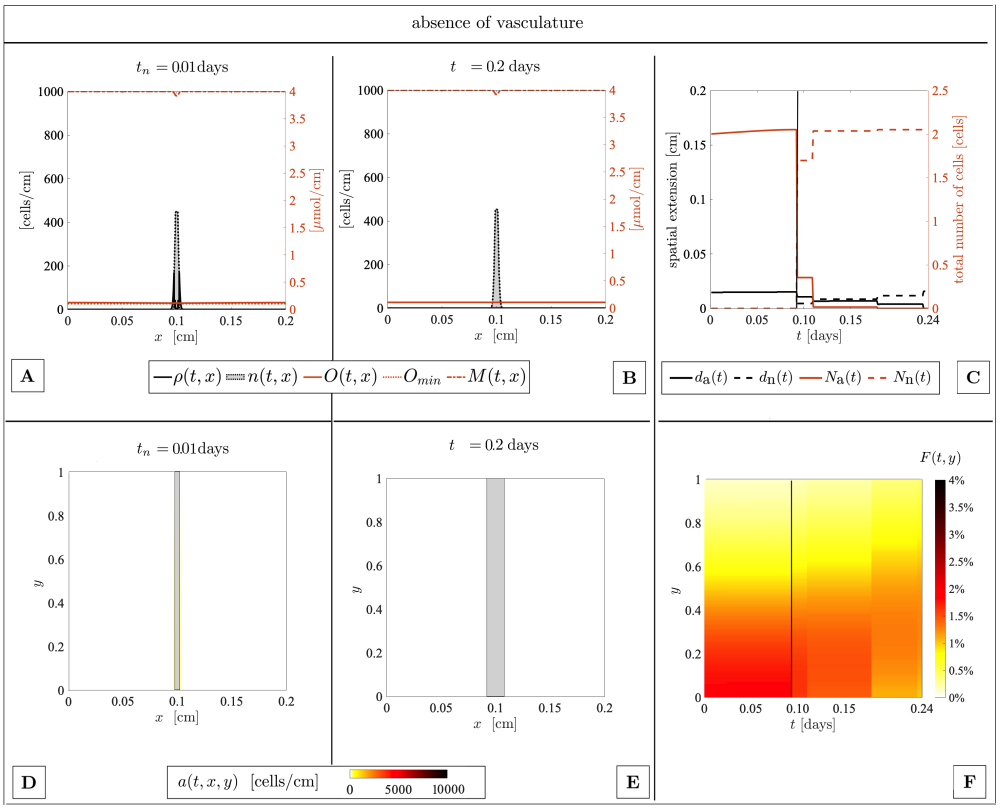

Figure 10: Tumor growth in the case of absence of functional vasculature, i.e., obtained by completing Eq. (12) with zero-flux boundary conditions. The lack of oxygen supply by the host results in an early necrosis, that quickly involves the entire mass. In panels (C) and (F), the black vertical line indicates t_n.

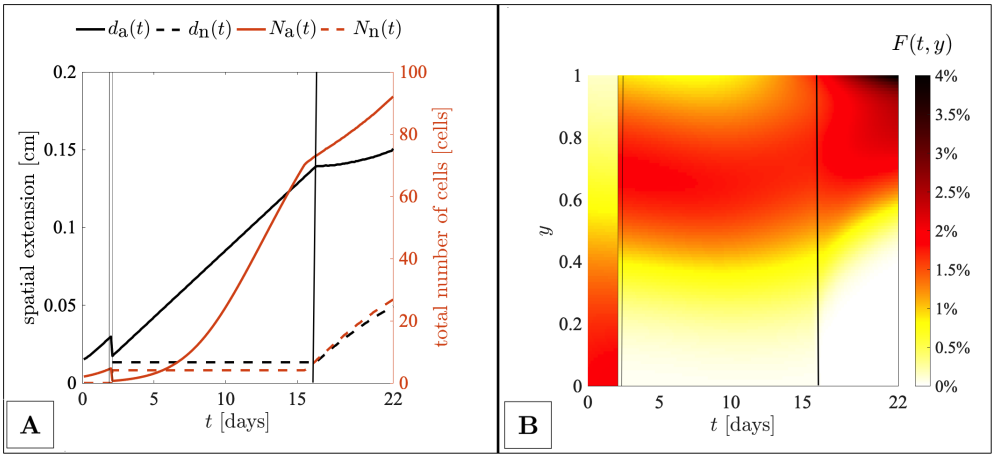

Figure 11: Tumor growth in the case of acute hypoxia, obtained by equipping Eq. (12) with time-dependent boundary conditions. In both panels, the thin black vertical lines indicate the extreme of the time-interval T_{hyp}, whereas the thick black vertical line indicate as usual t_n.

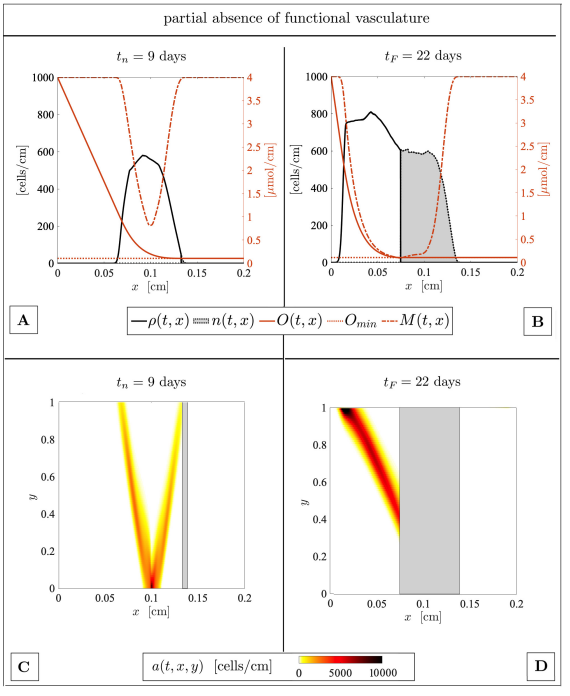

Figure 12: Tumor growth in the case of the presence of a functional vessel only at the left edge of the tissue. Such a scenario is obtained by completing Eq. (12) with a Dirichlet condition at the left boundary of the tissue and a Neumann zero-flux one at the right point edge. By splitting the spatial domain at the mid point $x = 0.1$ cm, we can almost observe the reference tumor progression on the left side and the evolution of the malignancy upon disrupted oxygen supply on the right side of the host.

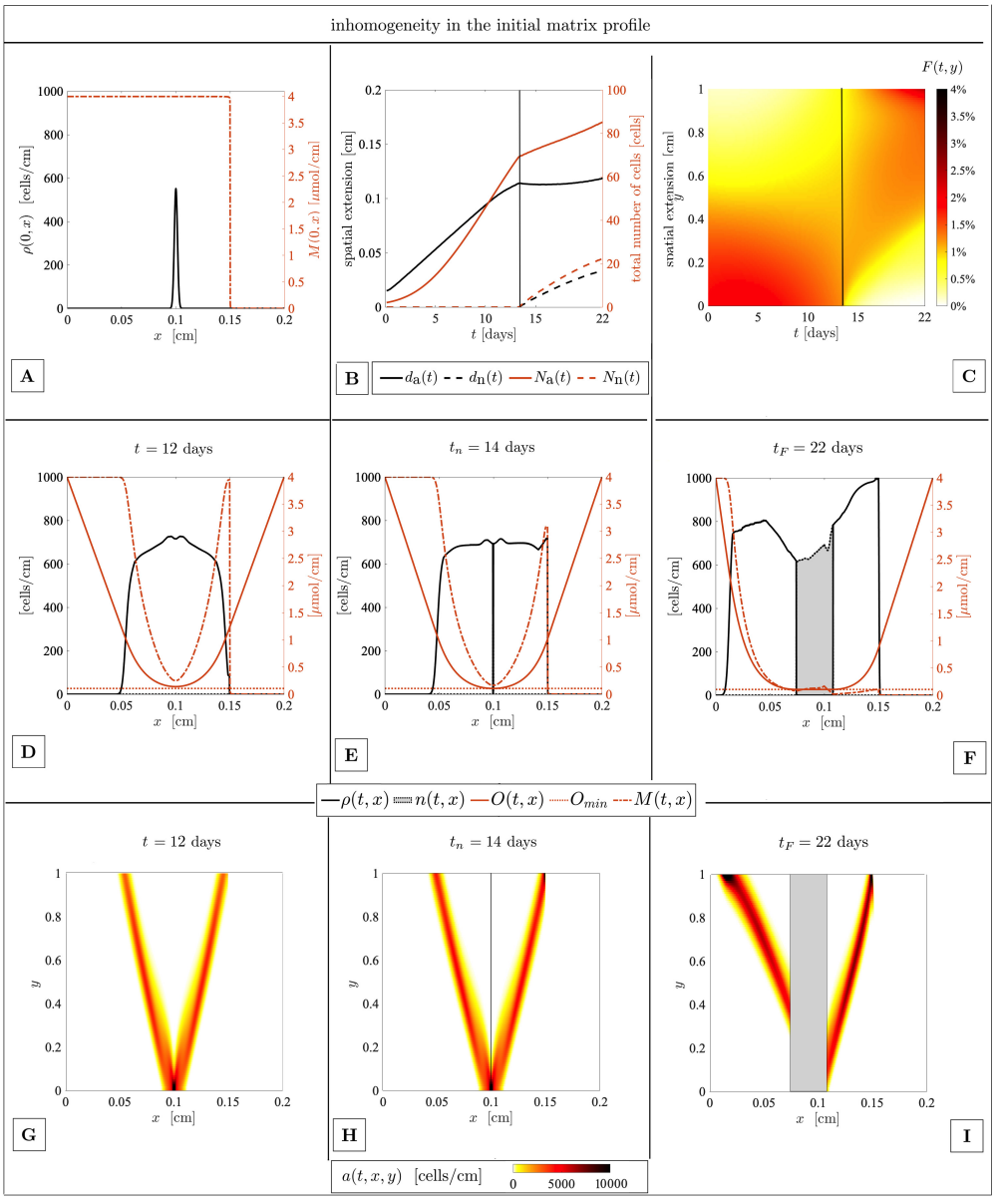

Figure 13: Tumor growth in the case of spatial inhomogeneity of initial matrix profile, defined in Eq. (19). The left portion of the malignant mass evolves as in the reference case. The right fraction instead normally progresses for 12 days, until its aggressive edge reaches the valley of ECM density. It then stops invasion since highly motile cell variants experience two competing stimuli: pressure stresses in fact point outwards whereas the specific ECM gradient results in a haptotactic velocity with an inwards direction (i.e., towards the bulk of the mass). Late stages of tumor progression indeed amount in the reference evolution at the left part and an accumulation of cells belonging to the entire spectrum of phenotypes at the right part. In panels (B) and (C), the black vertical line indicates t_n.